Research Square

Preprints are preliminary reports that have not undergone peer review.
They should not be considered conclusive, used to inform clinical practice,
or referenced by the media as validated information.

# Spatial biology of human follicular lymphoma

**Michael Green**

MGreen5@mdanderson.org

University of Texas MD Anderson Cancer Centre https://orcid.org/0000-0001-6309-9472

**Yoshiaki Abe**

University of Texas MD Anderson Cancer Centre

**Bijal Thakkar**

University of Texas MD Anderson Cancer Centre https://orcid.org/0000-0001-6202-7784

**Atish Kizhakeyil**

University of Texas MD Anderson Cancer Centre

**Andrew Feldman**

Mayo Clinic https://orcid.org/0000-0001-5009-4808

**Jared Henderson**

University of Texas MD Anderson Cancer Centre https://orcid.org/0000-0002-5121-5234

**Amy Ayers**

University of Texas MD Anderson Cancer Centre

**Ashley Wilson**

University of Texas MD Anderson Cancer Centre

**Robert Harkins**

University of Texas MD Anderson Cancer Centre https://orcid.org/0000-0003-2231-3940

**Priya Lakra**

University of Texas MD Anderson Cancer Centre

**Daisuke Kaji**

Toranomon Hospital https://orcid.org/0000-0002-9256-609X

**Ricky Nelles**

Mater Hospital

**Jonathan Cohen**

Emory University

**David Russler-Germain**

Washington University St. Louis https://orcid.org/0000-0003-1009-2247

**Eric Mou**

University of Iowa

**Francisco Vega**

MD Anderson Cancer Center https://orcid.org/0000-0001-5956-452X

**Jennifer Chapman**
University of Miami
**Giorgio Inghirami**
Weill Cornell Medicine https://orcid.org/0000-0001-5566-0864
**Carla Casulo**
University of Rochester Medical Center
**Izidore Lossos**
University of Miami https://orcid.org/0000-0002-9346-9013
**Jean Koff**
Emory University https://orcid.org/0000-0003-4414-0489
**Chijioke Nze**
University of Texas MD Anderson Cancer Center
**Peter Martin**
New York University
**Sergei Syrbu**
University of Iowa
**Kiran Vij**
Washington University in St. Louis
**David Jaye**
Emory University https://orcid.org/0000-0001-7977-6909
**Anne Novak**
Division of Hematology, Mayo Clinic, Rochester, MN https://orcid.org/0000-0002-7904-1651
**Richard Burack**
University of Rochester Medical Center https://orcid.org/0000-0002-5584-584X
**Matthew Maurer**
Mayo Clinic https://orcid.org/0000-0002-1867-0526
**Dai Chihara**
University of Texas MD Anderson Cancer Center https://orcid.org/0000-0002-1153-2294
**Mamiko Sakata-Yanagimoto**
University of Tsukuba https://orcid.org/0000-0001-7310-8045
**Oliver Weigert**
LMU University Hospital, LMU Munich https://orcid.org/0000-0002-0987-7373
**Joshua Tobin**
University of Queensland
**James Cerhan**
Mayo Clinic College of Medicine and Science https://orcid.org/0000-0002-7482-178X
**Christopher Flowers**
University of Texas MD Anderson Cancer Center
**Xubin Li**

University of Texas MD Anderson Cancer Center https://orcid.org/0000-0003-1727-9215

**Resource**

**Keywords:**

**Posted Date:** November 26th, 2026

**DOI:** https://doi.org/10.21203/rs.3.rs-11406874/v1

**License:** This work is licensed under a Creative Commons Attribution 4.0 International License.
Read Full License

**Additional Declarations: Yes** there is potential Competing Interest. M.R.G. reports research funding from Sanofi, Kite/Gilead, Abbvie, and Allogene; consulting for Allogene, Johnson & Johnson, Arvinas and Bristol Myers Squibb; honoraria from Esai, Chugai and MD Education; and stock ownership of Melbridge Therapeutics and Shenandoah Therapeutics. | I.S.S reports royalties or licenses: Stanford-Royalties; Receipt of equipment, materials, drugs, medical writing, gifts or other services: NCI, ADC Therapeutics (specifications: research funding). | J.B.C. reports current employment with Emory University in Atlanta, GA; reports a consulting or advisory role within BeiGene, Lilly, Astra Zeneca, Janssen, Genentech, Kite/Gilead; reports research funding from Genentech, Celgene, Novartis, Takeda, Astra Zeneca, Loxo/Lilly, Lam Therapuetics, BioInvent. | P.M. reports consulting fees from Abbvie, AstraZeneca, Beigene, BMS, Daiichi, Genentech, Janssen, Pepromene, Merck. | B.S.K. reports consulting fees including expert testimony from Astrazeneca, ADCT Therapeutics, Roche, Genetech, Abbvie, MEI, Celgene/BMS, Kite, BeiGene, Seattle Genetics, Lilly; reports payment or honoraria for lectures, presentations, speakers bureaus, manuscript writing or educational events with Research To Practice; reports research funding with Genetech, Abbvie, BeiGene, Astra Zeneca. | D.C. reports payment or honoraria for lectures, presentations, speakers bureaus, manuscript writing or educational events with ONO pharmaceutical, Genmab, BeiGene. | A.N. reports research funding from BMS. | G.L reports honoraria not related to the manuscript– AbbVie, ADC, AstraZeneca, BeOne, Bristol Myers Squibb, Eli Lilly, Exscientia, Flindr, Genmab, Gilead, GSK, Hexal/Sandoz, Incyte Corporation, Miltenyi, MSD, Novartis, PentixaPharm, Pierre Fabre, Roche, Sobi. Consultant/advisory boards not related to the manuscript – AbbVie, ADC, AstraZeneca, BeOne, Bristol Myers Squibb, Eli Lilly, Exscientia, Flindr, Genmab, Gilead, GSK, Hexal/Sandoz, Incyte Corporation, Miltenyi, MSD, Novartis, PentixaPharm, Pierre Fabre, Roche, Sobi. Research support not related to the manuscript– AbbVie, AstraZeneca, Gilead, Novartis, Sobi. | C.R.F. reports consulting fees from Bayer, Gilead, Spectrum Pharmaceuticals, AbbVie, Celgene, Denovo Biopharma, BeiGene, Karyopharm Therapeutics, Pharmacyclics/Janssen, Genentech/Roche, Epizyme, Genmab, SeaGen, Foresight Diagnostics, BMS/Celgene, Curio Science, AstraZeneca, MorphoSys; reports stock or stock options with Foresight Diagnostics, N Power; reports research funding from Acerta Pharma, Janssen Oncology, Gilead Sciences, Celgene, TG Therapeutics, Genentech/Roche, Pharmacyclics, AbbVie, Millennium, Alimera Sciences, Xencor, 4D Pharma, Adaptimmune, Amgen, Bayer, Cellectis, EMD Serono,

Guardant Health, Iovance Biotherapeutics, Kite/Gilead, MorphoSys, Nektar, Novartis, Pfizer, Sanofi, Takeda, ZIOPHARM Oncology. | J.R.C. reports all support for the present manuscript with Genentech; reports Mayo Clinic consulting fees with BMS – Connect Lymphoma Scientific Advisory Board, reports personal consulting fees with Protagonist Therapeutics SMC; reports research funding with Genmab, BMS. | K.K. reports consultanting for AbbVie, ADC Therapeutics, BeOne, Foresight Diagnostics, Incyte, and Pierre-Fabre.

# Spatial biology of human follicular lymphoma

Yoshiaki Abe[1,2]*, Bijal Thakkar[1,2]*, Atish Kizhakeyil[1,2]*, Andrew L. Feldman[3], Jared Henderson[1,2], Amy Ayers[1,2], Ashley Wilson[1,2], R. Andrew Harkins[1,2], Priya Lakra[1,2], Daisuke Kaji[4], Ricky Nelles[5], Jonathon B. Cohen[6], David Russler-Germain[7], Eric Mou[8], Francisco Vega[9], Jennifer Chapman[10], Giorgio Inghirami[11], Carla Casulo[12], Izidore S. Lossos[13], Jean L. Koff[6], Chijioke Nze[1,2], Peter Martin[14], Sergei Syrbu[15], Kiran Vij[16], David L. Jaye[17], Anne J. Novak[18], Richard Burack[19], Matthew J Maurer[20], Dai Chihara[1,2], Mamiko Sakata-Yanagimoto[21], Oliver Weigert[22], Joshua W.D. Tobin[5,23], James R. Cerhan[20], Christopher R. Flowers[1,2], Xubin Li[1,2,#], Michael R. Green[1,2,24,#]

[1]Department of Lymphoma & Myeloma, University of Texas MD Anderson Cancer Center, Houston, Texas, USA;

[2]Lymphoid Malignancies Program, University of Texas MD Anderson Cancer Center, Houston, Texas, USA;

[3]Department of Laboratory Medicine & Pathology, Mayo Clinic, Rochester, Minnesota, USA;

[4]Department of Hematology, Toranomon Hospital, Tokyo, Japan;

[5]Mater Research Institute, University of Queensland, Brisbane, Queensland, Australia

[6]Department of Hematology and Medical Oncology, Winship Cancer Institute, Emory University, Atlanta, Georgia, USA;

[7]Division of Oncology, Department of Medicine, Washington University School of Medicine, St. Louis, MO, USA;

[8]Department of Internal Medicine, Division of Hematology, Oncology, and Bone & Marrow Transplantation, University of Iowa, Iowa City, Iowa, USA;

[9]Department of Hematopathology, The University of Texas MD Anderson Cancer Center, Houston, Texas, USA;

[10]Department of Pathology, Division of Hematopathology, Sylvester Comprehensive Cancer Center, University of Miami, Miami, Florida, USA;

[11]Department of Pathology, Weill Cornell School of Medicine, New York, NY, USA;

[12]Department of Medicine, Wilmot Cancer Institute, University of Rochester, Rochester, NY, USA;

[13]Department of Medicine, Division of Hematology, Sylvester Comprehensive Cancer Center, University of Miami, Miami, Florida, USA;

[14]Department of Medicine, New York University, New York, New York, USA;

[15]Department of Pathology, University of Iowa, Iowa City, Iowa, USA;

[16]Department of Pathology, Washington University School of Medicine, St. Louis, Missouri, USA;

[17]Department of Pathology and Laboratory Medicine, Emory University, Atlanta, Georgia, USA;

[18]Division of Hematology, Mayo Clinic, Rochester, Minnesota, USA;

[19]Department of Pathology, University of Rochester, Rochester, New York, USA;

[20]Department of Quantitative Health Sciences, Mayo Clinic, Rochester, Minnesota, USA;

[21]Department of Hematology, Institute of Medicine, University of Tsukuba, Tsukuba, Japan;

[22]LMU Munich, Munich, Germany;

[23]Princess Alexandra Hospital, Brisbane, Queensland, Australia

[24]Department of Hematopoietic Biology and Malignancy, University of Texas MD Anderson Cancer Center, Houston, Texas, USA.

*These authors contributed equally.

[#]Correspondence: mgreen5@mdanderson.org (M.R.G.), XLi27@mdanderson.org (X.L.).

## ABSTRACT

Follicular lymphoma (FL) is the most common indolent B-cell lymphoma, with marked clinical heterogeneity and management ranging from active surveillance (AS) to immediate immunochemotherapy. However, FL's clinical heterogeneity remains unreconciled with disease biology. We generated a single-cell reference atlas from 166 FL tumors and applied spatial transcriptomics to 365 FL tumors to resolve lymphoma microenvironment (LME) niches. These orthogonal approaches identified CXCL13-expressing macrophages enriched within and around neoplastic follicles, termed follicular macrophages (FMs). FMs colocalized with proliferating follicular B cells predicted to be driven by FM-derived CXCL13 and APRIL. Matrix factorization resolved intrafollicular FL Archetypes of MicroEnvironment (FLAMEs) with diverse LME composition, including an FM-enriched FLAME. FM-FLAME was associated with histologic grades 3A and 3B, more frequent immunochemotherapy, and early progression under AS. These findings define cellular and spatial heterogeneity in FL and provide a clinicobiologic framework linking an FM-enriched ecosystem to B-cell proliferation, histology, and treatment.

## INTRODUCTION

Follicular lymphoma (FL) is the most common indolent lymphoma and exhibits substantial biological and clinical heterogeneity underpinning diverse management and treatment paths[1]. Histomorphological characteristics together with disease burden and patient symptoms contribute to a clinical spectrum of disease that informs treatment selection. Patients with lower-risk disease may be managed without treatment (commonly referred to as "active surveillance" [AS]) or with single-agent anti-CD20 antibody (e.g., rituximab [R]), whereas patients with more aggressive disease may receive immunochemotherapy (IC),

either with an anthracycline-sparing regimen (e.g., bendamustine + R [BR]) or an anthracycline-containing regimen (e.g., R + cyclophosphamide, doxorubicin, vincristine and prednisone [R-CHOP]), based on the perceived aggressiveness of the disease and risk of histological transformation[2]. Although approximately 40% of patients treated with R-CHOP require no further treatment[3], less intensive approaches can often lead to overall survival equivalent to age-matched healthy controls[4], and outcomes of FL patients have steadily improved over the decades[1]. However, a subset of patients have rapid progression and inferior long-term outcomes, with or without aggressive histologic transformation[5,6]. There thus exists a clinical conundrum in FL, balancing the pursuit of cure with the avoidance of unnecessary toxicity associated with intensification of therapy. This is not addressed by current clinical and biological systems to stratify patients. Although some efforts have been made to develop biologically centered risk scores that are predictive of patient outcomes[7,8], these are confounded in standard-of-care (SOC) populations by the diversity in therapeutic selection and the differential predictive power of outcome-supervised biomarkers across therapies.

FL is characterized by its distinctive histological architecture that maintains follicle-like structures harboring malignant B cells intermixed with lymphoma microenvironment (LME) cells, interspersed within interfollicular regions that are enriched for LME cells such as $CD4^+$ T cells. Histological features, including grade and features suggestive of transformation, are integrated with clinical prognostic indices that capture disease burden and symptoms to guide the choice of first-line therapy. FL exists on a histological continuum of grade 1/2 (FL1/2) with predominant centrocytes and low proliferative index, grade 3A (FL3A) with mixed centroblasts and centrocytes, and 3B (FL3B) with solid sheets of centroblasts typically accompanied by a high proliferative index. FL3B accounts for 5-10% of FLs, is often excluded from clinical trials, and is most frequently treated with R-CHOP based upon historical perspectives. FL3B is now referred to as follicular large B-cell lymphoma by the World Health Organization (WHO)[9,10] and has become a topic of controversy. Moreover, mechanisms underpinning FL histologic grade and relationships between its broad biological spectrum and the LME remain unknown[10] limiting the use of biology to guide treatment.

Here, we performed single-cell transcriptomics to define the cellular landscape of FL across 158 patients and resolve these populations spatially using highly multiplexed spatial molecule imaging (SMI) in an independent SOC cohort of 365 newly diagnosed FLs. We discovered marked diversity within the myeloid compartment of FL, exemplified by a microenvironment archetype enriched for follicular macrophage (FM) populations that were associated with proliferating B (PB) cells. Patients with FM-enriched LME more frequently had FL3A and FL3B, were more often treated with IC, and had worse outcomes when managed with AS. These data therefore outline a biological-clinical paradigm for FL in which

the spatial assembly of macrophages with PB cells associates with histologic grade and treatment selection.

## RESULTS

### Comprehensive cellular and spatial characterization of FL

Although the importance of the LME in FL is known, prior single-cell studies have not captured the full cellular composition of FL[11-14], and current spatial transcriptomics approaches are underpowered for cell type discovery due to data sparsity[15]. We therefore first mapped the cellular landscape of FL using single-nucleus RNA sequencing (snRNA-seq) of 65 newly diagnosed and 101 relapsed tumors from 158 patients (**Figure 1A; Figure S1A,B; Table S1**), totaling 1,429,860 cells after stringent quality control (**Figure 1B-C**). This allowed sensitive transcriptomic characterization of previously observed diversity in the $CD4^+$ and $CD8^+$ T cell compartments[11,12] together with remarkable heterogeneity in the myeloid and non-hematopoietic cell compartments (**Figure 1B–F; Figure S1C,D; Tables S2–11**). Cell type frequencies were not significantly different between newly diagnosed and relapsed tumors (**Figure 1E**), indicating a consistency in LME biology throughout the course of disease. Within the B-cell compartment, PB cells, quiescent malignant B cells (QMB), non-malignant B (nmB) cells, plasma cells (PCs), and a small fraction of unclassifiable B (UB) cells were identified using clustering plus B cell receptor clonotype sequences and inferred copy number profiles from snRNA-seq (**Figure 1D; Figure S1E,F; Table S12**). PB cells showed higher expression of genes that are characteristics of centroblasts such as *AIDCA* and *BCL6* (**Figure S1F**). The fraction of PB cells correlated with histologic grade (**Figure S1G**) but was not significantly different between newly diagnosed and relapsed diseases (**Figure S1H**).

Having compiled a comprehensive FL cellular reference, we extended our analysis to spatial molecular imaging (SMI) of 6,175 genes with a Bruker CosMx instrument in a multi-center cohort of 365 newly diagnosed FLs, comprising a SOC population from the Lymphoma Epidemiology of Outcomes cohort study[16] (n=304) and a cohort of FLs with low tumor burden (n=61) (**Figure 2A; Figure S2A; Tables S13-14**). All cases underwent clinical and hematopathology review and were assembled onto tissue microarrays (TMAs) for analysis, with SMI fields-of-view (FOVs) arranged to cover the entire core. The sampling bias during TMA construction is therefore similar to that associated with FOV selection from excisional biopsies, but the use of TMAs allows for high-throughput analysis of large sample sizes that would be cost-prohibitive for individual biopsies. Tumors included FL1/2 (n=275), FL3A (n=59), FL3B (n=14) and cases with unknown grade (n=17), and captured the clinical heterogeneity in first-line treatment selection (**Figure 2B**). Cell segmentation was performed

with an 8-antibody cocktail and supervised cell typing performed using our FL reference atlas to capture 54/58 LME cell subsets across 3,960,412 high-quality cells, with similar relative abundance and gene expression profile in SMI and snRNA-seq datasets (**Figure 2C–E**; **Figure S2B–D,S3; Tables S15–24**). B cells were classified by single-tumor cluster-level assignment according to immunoglobulin light-chain expression, and proliferation or PC marker genes (**Figure 2F; Figure S2E-F; Table S25**), then visually confirmed by the follicular localization of QMB and PB cells, perifollicular distribution of nmB cells, and interfollicular pattern for PCs (**Figure 2G**). QMB and PB were therefore used to mask neoplastic follicles, enabling assessment of the spatial distribution of LME cell types according to their distance to the follicle (**Figure 2H-I; Figure S4A-B).** This showed expected patterns for cell types known to localize to follicles, such as follicular dendritic cells (FDC) and T follicular helper (TFH) cells (**Figure 2I; Figure S4B-C)**. However, it also highlighted unexpected macrophage subsets enriched within neoplastic follicles, including two subsets with shared signature genes with or without additional expression of immediate-early genes (IEGs), which we named follicular macrophages (FM, FM_IEG; (**Figure 2I-J**; **Figure S4B,D**). Notably, cycling macrophages (Mac_Cycl) were also enriched within follicles. Together these data provide comprehensive cellular and spatial atlases of FL that identify a unique expansion of follicle-resident macrophages.

**Spatial association of follicular macrophages with proliferating B cells**

To identify recurrent spatial assemblies of cells, we defined cellular niches (CNs) by clustering local cellular neighborhoods composed of the 20 nearest neighboring cells. This approach identified 10 discrete CNs, each characterized by distinct cellular compositions and gene expression profiles of major cell subsets (**Figure 3A–E**). Most CNs (CN2–8) corresponded to recognizable cellular assemblies and tissue structures characteristic of non-malignant lymphoid tissue, with variable admixture of QMB cells (**Figure 3A,E**). However, CN1 represented a unique collection of multiple macrophage subsets together with PB cells (**Figure 3A,F**). To validate the spatial co-localization of macrophage subsets with PB cells, we quantified the proportion of LME cell subsets among the 20 nearest neighboring cells surrounding either PB or QMB cells relative to background (intrafollicular regions). While follicle-resident TFH cells and FDCs were enriched around both PB and QMB cells, multiple macrophage subsets including FM, FM_IEG, Mac_*CHIT1*$^{+}$, and Mac_Cycl were significantly enriched around PB cells but under-represented around QMB cells (**Figure 3G**). Reciprocal analysis assessing the relative enrichment of cells neighboring macrophage subsets similarly showed significant enrichment of PB cells and depletion of QMB cells around FM, FM_IEG, Mac_*CHIT1*$^{+}$, and Mac_Cycl subsets (**Figure 3H**).

The distinctive architecture of FL may bias towards discovery of CNs that are associated with the normal intrafollicular and interfollicular arrangement of cell subsets, obscuring biologically relevant patterns of spatial organization within neoplastic follicles. We therefore performed an independent analysis focused on intrafollicular regions, using the top 50% of LME cell subsets ranked by follicular proximity (lowest follicle distance, **Figure 2I**), which successfully excluded known interfollicular cell subsets. Because malignant B cells were used to define the neoplastic follicle boundaries, they were not included within the cell subsets used for archetype discovery. Non-negative matrix factorization (NMF) clustering of intrafollicular cell fractions for these cell subsets across tumors identified five FL Archetypes of MicroEnvironment (FLAMEs), annotated according to their predominant LME cell subsets (**Figure 4A–D**); each sample was assigned to a single FLAME by NMF clustering and visually confirmed with available protein markers from the same sample (**Figure 4E**). The FM-FLAME (13.1% of FL cases) was characterized by enrichment of macrophage subsets, including FM, FM_IEG, Mac_*CHIT1*$^+$, and Mac_Cycl that were enriched in CN1; follicular stroma (FS)-FLAME (16.0%) was enriched for FDCs and marginal reticular cells (MRCs); TFH-FLAME (27.7%) was enriched for TFH and T regulatory ($T_{reg}$) cells; cytotoxic T (CYT)-FLAME (28.3%) was enriched for cytotoxic T cell populations, including CD4$^+$ cytotoxic and CD8$^+$ follicular cytotoxic subsets together with exhausted CD8$^+$ T cells; nmB-FLAME (14.9%) was marked by enrichment of nmB cells (**Figure 4D–E**). The ratios of PB to B or all cells were significantly higher in FM-FLAME tumors compared to others (**Figure 4F**), but the total fraction of tumor B cells was not significantly different except when compared to the nmB-FLAME (**Figure 4G**), providing tertiary validation of an association between follicular macrophage-enriched spatial niches and proliferation of FL B cells. Consistent with this finding, FM-FLAME tumors exhibited higher proliferation scores and larger cell size for malignant B cells, and higher proportions of CN1 compared with non-FM-FLAME tumors (**Figure 4H–J**). Somatic mutations were not significantly associated with FM, FM_IEG, or Mac_Cycl proportions, CN abundances, or FLAMEs (**Figure S5A–F**). Together, these data and orthogonal analytical methodologies demonstrate that PB cells in FL spatially co-segregate with unique macrophage populations.

## Cellular origins and cell-cell interactions of follicular macrophages

The observed spatial heterogeneity among macrophage subsets and their association with PBs prompted us to investigate the predicted origins and signaling drivers of macrophage populations within the FM-FLAME. Differentially expressed genes (DEGs) from macrophage subsets highlighted high expression of inflammatory macrophage genes such as *ITGAX* (CD11c), *IL21R*, *TLR4*, in FM and FM_IEG cells, together with expression of *CXCL13*, which

serves as a chemoattractant for CXCR5$^+$ B cells in the dark zone of the germinal center[17-20] (**Figure 5A; Tables S5,18**). However, FM and FM_IEG cells did not express genes that are characteristic of tingible body macrophages (*MERTK*, *CX3CR1*), which typically have large cell size and reside within the germinal center dark zone (**Figure 5A; Tables S5,18**), consistent with the moderate sizes of follicular macrophages (**Figure S6A**) and low frequency of tingible body macrophages observed in follicular macrophage-rich FL specimens compared to tonsil tissue (**Figure S6B**). FM_IEG cells expressed immediate early genes (*JUN*, *ATF3*), whereas FM cells lacked these features and likely represent the prototypic states of follicular macrophages (**Figure 5A**). FM and FM_IEG cells exhibited features that have been described in the context of tumor-associated macrophages (TAMs), including immunoregulatory genes (e.g., *TNFRSF11B*, *IGFBP2*, *SIGLEC15*) and tissue-remodeling genes (e.g., *SPARC*, *CHI3L1*, *MMP16*)[21-24] (**Figure 5A; Tables S5,18**), but their overall transcriptional profiles did not align with previously described macrophage subsets from the pan-tissue MoMac-VERSE reference dataset[25] (**Figure 5B–E; Figure S6C–E**). Specifically, follicular macrophage signature genes such as *IL21R*, *TNFSF13*, and *CXCL13* were not expressed by the previously defined macrophage subsets in MoMac-VERSE (**Figure 5C; Figure S6D**). Consistent with this distinction, FM cell signature genes showed poor correlation with established macrophage subset signatures (**Figure 5D**), and prediction scores for these subsets showed little alignment with the FM cell gene signature (**Figure 5E**). In contrast, tissue resident-like (TRL) macrophage subsets (TRL, TRL_IEG) shared expression of genes associated with tissue-resident macrophage phenotypes (e.g., *CD163*, *CD209*, and *MRC1*) and showed strong correlation with the MoMac-VERSE Mac_*HES1* subset (**Figure 5A,D,E; Figure S6E**). Given the unique nature of the follicular macrophages, we aimed to validate them in an independent spatial protein imaging (SPI) dataset of 242 FL samples[26] using the CD68 macrophage marker together with CXCL13 to identify the putative follicular macrophage counterpart (**Figure S6F–I**). This confirmed abundant CXCL13$^+$ macrophages within and around the neoplastic follicles of FL tumors (**Figure 5F**) that, together with Ki67$^+$ macrophages (corresponding to Mac_Cycl) (**Figure S6I**), exhibited shorter distances to follicles than the remaining macrophage population (**Figure S6J**).

To predict the origins of follicular macrophages, we used RNA velocity and pseudotime analysis of macrophages from snRNA-seq data. RNA velocity revealed directional transitions from TRL macrophages toward terminal macrophage states of FM and FM_IEG cells, with TRL_IEG occupying an intermediate position along the FM_IEG trajectory (**Figure 5G**). Consistently, trajectory analysis revealed a structured continuum among macrophage states, showing two major trajectories originating from TRL: one leading directly to FM cells and the other progressing through TRL_IEG before reaching FM_IEG (**Figure 5H**). To predict signals that were likely to drive follicular macrophage development, we performed cell-cell

communication (CCC) analysis of the FM-FLAME. Integrative ligand activity prediction and cell–cell interaction analyses using orthogonal approaches with NicheNet[27] and CellPhoneDB and orthogonal datasets with snRNA-seq and SMI data to identify consensus predictions. Given the follicle-biased spatial distribution of FM cells, the analysis included LME cell subsets preferentially localized within intrafollicular regions and enriched around FM cells (**Figure 3H**). NicheNet analysis of both SMI and snRNA-seq datasets identified multiple signals predicted to drive FM cell signature genes, such as TGFB1 originating from rare classical and plasmacytoid dendritic cell subsets, and signals from abundant intrafollicular cell subsets such as IL34 from FDCs and CD40L from TFH cells (**Figure 5I; Figure S7A**). CellPhoneDB analysis likewise supported activation of the CD40L–CD40 axis[28] between TFH and FM cells (**Figure 5J; Figure S7B,C**), and the axis was spatially enriched within neighboring TFH and FM cells (**Figure 5K**). CD40L was among the top predicted regulators of TNFSF13 (APRIL) expression in FM cells (**Figure S7D**) and treatment of U937-derived macrophages with CD40L significantly increased the expression of TNFSF13 by ELISA (**Figure 5L**). IL34 expressed by FDCs and colony stimulating factor 1 (CSF1) expressed by FDCs, $T_{reg}$ cells, and exhausted $CD8^+$ T cells were also predicted to be prominent drivers of the CSF1R-expressing FM cells (**Figure 5I-J**), representing a potential therapeutically targetable axis for the FM-FLAME[29].

We further evaluated potential CCC pathways between FM and PB cells, using DEGs upregulated in PB cells from FM-FLAME compared with non-FM-FLAME samples for NicheNet analysis, which included proliferation and cell survival programs of PB cells (**Figure S7E; Table S27**). Interestingly, APRIL[30] was consistently identified as a potential ligand regulating PB cell signature genes (**Figure 5M; Figure S7F**). APRIL has been reported to induce proliferation of malignant B cells in FL and other B-cell lymphomas[31,32], and *TNFSF13* was highly expressed by follicular macrophages in both snRNA-seq and SMI datasets (**Figure 5A,M; Figure S3,S7F**). CellPhoneDB analysis further supported interactions mediated through FM cell-derived TNFSF13 to PB cells (**Figure 5N; Figure S7G-H).** The well-characterized CXCL13–CXCR5 axis[19,20,33], mediated through FM cell-derived CXCL13, was also predicted to be active in signaling to PB cells (**Figure 5M-N; Figure S7F–H).** Together, this uncovers a multicellular LME-tumor axis in FL, implicating TFH-derived CD40L in the induction of follicular macrophage-derived TNFSF13 and CXCL13 that signal to malignant PB cells (**Figure 5O**).

## FM-FLAME associates with histologic grade and treatment selection

We next investigated the clinicopathological relevance of FLAMEs in 343 patients with previously untreated FL and complete clinical annotation. FM-FLAME showed a striking

association with histologic grade determined in routine clinical assessment, with more than half (57.1%) of FL3B cases classified as FM-FLAME, and more than half of FM-FLAME cases being FL3A (34.9%) or FL3B (18.6%) (**Figure 6A**). This is consistent with the larger size of malignant B cells and higher proportion of PB cells in the FM-FLAME compared to other FLAMEs (**Figure 4F,I**). Furthermore, FM-FLAME tumors were more commonly BCL2 negative at the protein level (**Figure 6B-C**), consistent with the frequent BCL2 negative status of FL3B tumors[34-36] (**Figure 6B**).

FLAMEs were not strongly associated with factors of the FL International Prognostic Index (FLIPI) or Groupe d'Etude des Lymphomes Folliculaires (GELF) criteria[37]; however, the FM-FLAME was significantly associated with elevated serum lactate dehydrogenase (LDH) levels, potentially reflecting increased cellular turnover and metabolic activity of malignant B cells (**Figure S8A–K**). Consistently, patients with FM-FLAME were more frequently treated with IC than patients with other FLAMEs (**Figure 6D**), particularly with anthracycline-containing R-CHOP (**Figure 6E**). In contrast, patients with nmB-FLAME were more frequently managed by AS (**Figure 6D**). In line with the propensity for initial treatment of FM-FLAME tumors, the small number of patients with FM-FLAME managed with AS had shorter event-free survival (EFS) than those with non-FM-FLAME, but no association with EFS was observed in patients treated with IC when comparing FM- versus non-FM-FLAMEs (**Figure 6F; Figure S8L**). Characterized by follicular macrophages and PB cells, CN1 provided a quantitative, integrated measurement of the malignant and non-malignant cellular constituents underlying the FM-FLAME. Accordingly, CN1 abundance was moderately associated with FLIPI risks (**Figure 6G**) and showed association with histologic grades FL3A and FL3B (**Figure 6H**), increased IC treatment assignment (**Figure 6I**), and reduced EFS in patients with AS but not in treated patients (**Figure 6J-K**).

To further support these findings using an independent cohort analyzed by an orthogonal spatial profiling technology, we re-analyzed published SPI data of FL[26] focusing on intrafollicular macrophages. We calculated intrafollicular macrophage percentage (IFMP) in the SMI dataset and evaluated its association with FM-FLAME. Receiver operating characteristic (ROC) analysis demonstrated excellent predictive performance of IFMP for FM-FLAME, with an area under the curve of 0.90 (**Figure 7A**; **Figure S9A**). We defined an IFMP cut-off value of 2.5% based on ROC analysis using the Youden approach (**Figure 7A**) and yielded high sensitivity (81.4%), specificity (84.0%), and negative predictive value (96.9%) for predicting FM-FLAME cases (**Figure 7B**) with similar proportions of high IFMP cases identified in SMI and SPI datasets (**Figure 7C**). Notably, patients with high IFMP recapitulated the clinicopathological features of FM-FLAME cases (**Figure 7D–F**; **Figure S9B–H**), with higher fractions of PB cells despite similar malignant B content (**Figure 7D-E**; **Figure S9I,J**) and strong associations with histologic grade and BCL2 negativity (**Figure 7F-G; Figure S9K**).

Furthermore, high IFMP was associated with shorter EFS in patients managed by AS, whereas no association with EFS was observed in treated patients (**Figure 7H**). Thus, IFMP provides orthogonal validation for the FM-FLAME, demonstrating that macrophage enrichment within intrafollicular regions is associated with PB cell enrichment and clinicopathological presentations of FL.

## DISCUSSION

Anchored to a large-scale snRNA-seq cellular atlas, our spatial characterization of FL uncovered previously unrecognized macrophage subsets and their assembly into compositionally and topologically defined compartments that reconcile FL biology with heterogeneous clinicopathologic features. Specifically, the spatial co-localization and sample-level co-occurrence of follicular macrophages with PB cells were associated with histological features and treatment selection. These findings therefore suggest that a follicular macrophage-rich LME within neoplastic follicles, rather than tumor cell-intrinsic features alone, contributes to aggressive FL biology.

Follicular macrophages were characterized by high expression of *CXCL13* and *TNFSF13*, as well as TAM-related features. CXCL13 expression is classically associated with FDCs[38,39] and TFH cells[40], whereas CXCL13-expressing macrophages have been reported only in limited inflammatory[41] and neoplastic[42-44] settings, and their biological significance remains incompletely defined. In addition, macrophage states spatially organized within follicular structures have scarcely been described. The absence of analogous follicular macrophages in the MoMac-VERSE atlas further supports the idea that these cells represent a unique follicular niche-associated macrophage state. Furthermore, the selective spatial association between follicular macrophages and PB cells raises the possibility that follicular macrophage-associated programs contribute to B-cell proliferation in normal and malignant lymphoid follicles, underlying their association with advanced histologic grade in FL.

APRIL-mediated interactions provide a plausible mechanism linking follicular macrophages to B-cell proliferation within the FM-FLAME. FDCs, which are known to provide B-cell activating factor (BAFF)-mediated survival signal to B cells[33,39], and TFH cells, which are known to provide CD40L costimulation to B cells, were spatially enriched around both QMB and PB cells in FL. In contrast, follicular macrophages were selectively enriched around PB cells and highly expressed *TNFSF13* (APRIL). These observations suggest that, whereas BAFF may broadly support FL B-cell survival, APRIL may contribute more specifically to proliferation centers, consistent with prior evidence that APRIL can directly enhance FL B-cell proliferation[32]. Furthermore, FL is characterized by an unusually TFH-rich LME[26,33],

raising the possibility that TFH-derived signals such as CD40L contribute to the deregulated establishment of follicular macrophage states in FL. Integrating the spatial, transcriptional, and CCC findings, we propose a model in which a TFH–FM–PB axis contributes to a proliferative FL ecosystem.

Importantly, histologic grades in FL have been defined based on the morphology and abundance of centroblastic cells, with the underlying biological mechanisms and associated clinical phenotypes remaining elusive. FL3B, also called follicular large B-cell lymphoma[45], is recognized as a distinct clinicopathological entity defined by centroblast-rich morphology, characterized by relatively aggressive clinical behavior. FL3A occupies a histological position between FL1/2 and FL3B[33,45], indicating that a subset of FL3A cases likely share FL3B biological programs. Our study provides insights into this long-standing question by presenting orthogonal lines of evidence implicating follicular macrophages as a key driver of malignant B-cell proliferation and associated advanced histologic grade. The relevance of follicular macrophages to FL biology is further supported by a previous report linking increased intrafollicular macrophage counts to inferior outcomes in pre-rituximab era[46]. In line with the higher frequency of FL3A and FL3B cases, we noted an increased selection of IC as first-line therapy for FL with FM-FLAME. Although it is difficult to extricate this association from other factors that inform treatment decisions such as serum LDH, which were also associated with the FM-FLAME, we have uncovered a paradigm for FL that may underlie the intuitive clinical management of some patients and can be formalized.

Current spatial analyses are inherently limited by their reliance on selected two-dimensional tissue regions, potentially incompletely capturing rare or spatially restricted cell states and intratumoral microenvironmental heterogeneity. This is problematic when using TMAs because they represent small portions of the tumor that are selected by a pathologist and therefore may have biases towards certain features. Sampling bias is also introduced in spatial transcriptomics approaches, which utilize FOV selection. To mitigate these limitations, we analyzed a large FL cohort and integrated orthogonal layers of evidence across complementary technologies and analytical approaches. Preclinical models of FL are limited[47]; therefore, future studies leveraging tissue-wide and three-dimensional spatial profiling should be complemented by improved experimental models to further refine the architecture of FL ecosystems and establish the biological functions of follicular macrophages and their role in organizing proliferative niches.

In conclusion, our highly multiplexed integrative spatial analysis of FL unveiled macrophage-centered cellular ecosystems associated with proliferative lymphoma niches and histological grade. Our findings suggest that clinically relevant aggressive FL phenotypes may be understood not solely as manifestations of malignant B-cell biology, but also as

emergent properties of spatially organized LME ecosystems. This framework provides a new perspective on the biological basis of FL progression and refines the current understanding of aggressive disease biology in FL.

## ONLINE METHODS

### Human samples

*snRNA-seq*

Lymphoma patient samples were collected after patients provided written informed consent under protocols approved by the Institutional Review Board of MD Anderson Cancer Center (Protocol PA19-0420). Tumor samples were obtained by core needle or excisional biopsy for diagnostic purposes, and residual tissue specimens were either snap-frozen without media or cryopreserved intact in fetal bovine serum containing 10% DMSO without prior tissue dissociation. Peripheral blood samples were obtained during routine clinical laboratory draws, processed to isolate peripheral blood mononuclear cells by Ficoll density-gradient centrifugation, and cryopreserved in fetal bovine serum containing 10% DMSO.

*CosMx SMI*

Patients aged 18 years or older with non-Hodgkin lymphoma were enrolled within six months of initial diagnosis into the Lymphoma Epidemiology of Outcomes (LEO) cohort study (NCT02736357) between July 1, 2015 and May 31, 2020 at one of eight participating centers: Emory University (Atlanta, GA), Mayo Clinic (Rochester, MN), MD Anderson Cancer Center (Houston, TX), University of Iowa (Iowa City, IA), University of Miami (Miami, FL), University of Rochester Medical Center (Rochester, NY), Washington University (St. Louis, MO), and Weill Cornell Medicine (New York, NY). Detailed descriptions of the cohort have been reported previously[16]. Briefly, all participants provided written informed consent, and the study was approved by all LEO institutional review boards (IRBs). Baseline clinical and treatment data were abstracted using a standard protocol, and all patients were prospectively followed for disease progression/relapse, new treatment, and death, with validation of these events against medical records. Most participants also provided peripheral blood samples, which were shipped to the LEO Biorepository at Mayo Clinic, where genomic DNA was extracted and stored.

A hematopathologist reviewed all cases and classified them according to the World Health Organization Classification of Tumours of Haematopoietic and Lymphoid Tissues[48], and selected cases with sufficient quality and quantity of material for coring. These materials were sent to the LEO Pathology Core at Mayo Clinic, where hematoxylin and eosin (H&E)-

stained sections were reviewed and annotated for coring by a hematopathologist (A.F.). Up to eight 1-mm cores were obtained from tumor-rich regions of each formalin-fixed paraffin-embedded (FFPE) block. Two cores were incorporated into each of two sister tissue microarrays (TMAs). TMAs were mixed across LEO centers, included replicate quality control samples (human tonsil).

FL tumor samples were also collected from Mater Hospital Brisbane (Australia). All patients provided written informed consent, and the study was approved by the relevant IRB. A 1.5-mm core was obtained from each FFPE black.

**Processing of patient samples for snRNA-seq**

Frozen tissue specimens (including snap-frozen and cryopreserved) were processed for snRNA-seq, using Chromium Next GEM Single Cell 5' (10x Genomics, 1000263). Cryopreserved tissue samples were placed in a 37C water bath and immediately transferred to NP40 lysis buffer on ice (10x Genomics, CG000375). Nuclei were released by mechanical dissociation using a gentleMACS Dissociator (Miltenyi Biotec, 130-095-937), filtered sequentially through 70-µm and 30-µm cell strainers, and washed in wash buffer (10x Genomics, CG000375). Following centrifugation, nuclei were resuspended in PBS containing 0.4% UltraPure BSA (Life Technologies, AM2616) and RNase Inhibitor (Sigma, 3335402001). Nuclei concentration was determined using a Countess II FL Automated Cell Counter (Thermo Fisher Scientific), and nuclei integrity was assessed by light microscopy. Nuclei suspensions were adjusted to the target concentration recommended by the manufacturer for recovery of approximately 10,000 nuclei per sample and immediately subjected to library preparation.

**Single-nucleus 5’ sequencing**

GEM generation and barcoding, as well as Gene Expression and BCR library construction, were performed according to the Chromium Next GEM Single Cell 5' Reagent Kits v2 protocol (CG000331 Rev E). Gene Expression and BCR libraries were constructed by amplifying cDNA fragments in a sample-indexing PCR using Amp Mix (10x Genomics, 2000047) and Dual Index TT Set A (10x Genomics, 3000431). The quantity and quality of all sequencing-ready libraries were assessed using High Sensitivity DNA ScreenTape analysis (Agilent Technologies) and the Qubit dsDNA HS Assay Kit (Thermo Fisher Scientific). Libraries were sequenced on an Illumina NovaSeq 6000 platform. Dual-indexed libraries (10-bp i7 and 10-bp i5 index reads) were sequenced using 100-bp paired-end reads (PE100), with a minimum sequencing depth

of 50,000 reads per nucleus for Gene Expression libraries and 5,000 reads per nucleus for BCR libraries.

**snRNA-seq data preprocessing**

The raw scRNA-seq reads were processed using Cell Ranger v9.0.1 (10x Genomics), which included demultiplexing cellular barcodes, aligning reads to the GRCh38 reference transcriptome (refdata-gex-GRCh38-2024-A), and generating gene expression feature-barcode matrices. Cell Ranger was executed with the --include-introns option to retain intronic reads and the --nosecondary option to skip secondary analyses, while BAM files were generated for downstream analyses. Samples containing fewer than 500 detected cells or with a mean sequencing depth below 30,000 reads per cell were excluded from downstream analyses. The resulting raw and filtered feature-barcode matrices were used for subsequent ambient RNA correction and downstream single-cell analyses.

**snRNA-seq data analysis**

*Cell identification and ambient RNA correction*

Using the raw and filtered feature-barcode matrices generated by Cell Ranger for each sample, ambient RNA contamination was corrected using SoupX (v1.6.2). Ambient RNA-corrected count matrices were generated using the adjustCounts function. Subsequently, the Scanpy pipeline (version 1.8.2) was applied to the count matrices of all samples for data processing, quality control (QC), normalization, dimensionality reduction, and unsupervised clustering.

*QC*

Genes detected in fewer than three cells and cells with fewer than 200 detected genes were excluded from the analysis. Additionally, cells with more than 15% of their transcript counts derived from the mitochondrial genome were discarded. Potential doublets predicted by scDblFinder (v1.16.0) were also removed. Furthermore, cells with more than 7,500 detected genes were eliminated to reduce the likelihood of doublet or multiplet captures. During downstream analysis after unsupervised clustering, potential doublets were identified in clusters that expressed canonical markers of distinct lineages, along with low-quality cells from clusters that exhibited significantly high levels of mitochondrial genes or ribosomal protein genes. These cells were subsequently discarded.

*Normalization, dimensionality reduction, clustering, and DEGs*

Each cell was normalized by total counts across all genes to ensure that every cell had the same total count of 10,000. The normalized data were then log2p1-transformed. The top 3,000 highly variable genes (HVGs) were selected, and their expressions were adjusted by regressing out the effects of total counts per cell and the percentage of mitochondrial genes. After scaling the data to unit variance with a zero mean for each gene, principal component analysis (PCA) was performed for dimensionality reduction, and the top 50 principal components (PCs) were retained for downstream analyses. Subsequently, Uniform Manifold Approximation and Projection (UMAP) embedding was calculated for cell visualization, and the Leiden algorithm was employed for unsupervised clustering of cells. DEG analysis was performed using the FindMarkers or FindAllMarkers functions of the Seurat package as appropriate. The DEGs were filtered to extract those expressed in at least 10% of cluster cells with an expression log2 fold change > 0.25 and an adjusted p value (based on the Bonferroni correction) of <0.05. The listed DEGs were used for the annotation of cell clusters by carefully reviewing the expression of canonical markers and immune cell-related functional genes along with an extensive literature search.

*Cell lineage annotation*

Initial cell-type labels were assigned to all cells using SingleR (v2.14.1) with the LymphoMAP[49] pseudobulk gene expression reference dataset. Predicted cell types were subsequently consolidated into four major lineage categories: B cells, non-B lymphoid cells, myeloid cells, and non-hematopoietic cells. To improve annotation consistency, lineage labels were refined using a k-nearest neighbor (kNN)-based label filtering strategy followed by random forest classification. Briefly, a kNN graph was constructed from the first 50 principal components using 50 nearest neighbors, and each cell was reassigned according to the majority lineage label among its neighboring cells when >50% agreement was achieved. Cells without a majority consensus were subsequently classified using a random forest classifier trained on the refined lineage labels. To establish robust lineage partitions, high-resolution Leiden clustering was performed and final lineage assignments were confirmed by examining cluster-specific differentially expressed genes together with canonical lineage marker genes.

*Non-B cell type annotation*

Each non-B lineage was independently analyzed to identify major cell types. Lineage-specific neighborhood graphs were constructed using 5–50 principal components, and Leiden clustering was performed at resolutions ranging from 0.1 to 1.0, with parameters selected according to the size and transcriptional complexity of each lineage. Cluster identities were assigned based on cluster-specific DEGs, canonical lineage marker genes, and published studies. Clusters exhibiting mixed or discordant lineage-specific gene-

expression profiles indicative of potential doublets were identified through DEG and marker-gene examination and removed from subsequent analyses. Clusters displaying a coherent transcriptional identity inconsistent with the compartment in which they were initially partitioned were reassigned to the appropriate cell-type compartment. Clustering, annotation, and cluster reassignment were iteratively repeated until stable and biologically consistent cell-type identities were obtained.

*Non-B cell subset annotation*

Each non-B cell type was independently sub-clustered to identify transcriptionally distinct cell subsets. Neighborhood graphs were constructed using 5–50 principal components, and Leiden clustering was performed at resolutions ranging from 0.1 to 1.0, with parameters selected according to the size and transcriptional complexity of each cell type. Cell subset identities were assigned based on cluster-specific DEGs, canonical marker genes, and published studies. Sub-clusters exhibiting markers indicative of distinct lineages, suggestive of potential doublets, were excluded from downstream analyses. Sub-clusters enriched for mitochondrial or ribosomal gene expression were also removed as low-quality populations.

*Single-cell BCR sequencing analysis*

Single-cell B-cell receptor (scBCR-seq) data were processed using Cell Ranger V(D)J v9.0.1 (10x Genomics) with the human V(D)J reference (refdata-cellranger-vdj-GRCh38-alts-ensembl-7.1.0) to assemble BCR contigs and generate per-cell receptor annotations. Immunoglobulin V, D and J germline genes were assigned using IgBLAST (v1.22.0) within the Immcantation framework (v4.8.0) for immunoglobulin (IG) loci. Sample-specific nearest-neighbor junction distance distributions were calculated using the Shazam package (v1.3.2) under a length-normalized Hamming distance model, and clone-defining distance thresholds were estimated independently for each sample using density-based threshold detection. Within each sample, BCR clonotypes detected in ≥2 cells were classified as expanded clonotypes. The constituent IGH, IGK, and/or IGL V–J gene combinations of these expanded clonotypes were used as reference patterns for cell-level matching. Individual cells were considered to match an expanded clonotype pattern when both the V and J gene assignments of an available IGH, IGK, and/or IGL chain matched a V–J combination present in the expanded clonotypes.

*Single-cell copy number variation analysis*

Copy number variation (CNV) was estimated in B cells at the single-cell level using inferCNV (v.1.25.0). For each sample, single-nucleus count matrices and initial cell-type annotations were used to classify cells into B cells and non-B cells. Non-B cells were used as the reference population, and B cells were analyzed as the observation population. Prior to

inferCNV-based evaluation, cells from each sample were subjected to log-normalization, scaling, PCA, and unsupervised clustering at a resolution of 1.0 using the Seurat workflow. inferCNV was then applied to infer large-scale chromosomal copy number alterations in B cells relative to non-B reference cells. Chromosomal regions showing the most prominent CNV variation were identified from inferCNV heatmaps. Chromosome-level CNV scores were calculated for each cell by averaging inferCNV expression values across genes located on the selected chromosome or chromosomal region. These scores were projected onto the existing UMAP embedding and examined together with sample-level unsupervised clusters. Cells in B-cell clusters showing coherent CNV signals were considered positive for CNVs, whereas cells in B-cell clusters lacking clear CNV signals were negative for CNVs.

*Classification of B cells*

B-cell identities were determined by integrating transcriptional clustering with BCR clonotype and CNV information. Malignant versus non-malignant B-cell status was determined by integrating inferCNV-derived copy-number profiles with the expanded BCR clonotype pattern matching described above. Matching to an expanded BCR clonotype pattern or the presence of inferCNV-derived large-scale copy-number alterations was considered evidence of malignancy. B cells meeting either criterion were classified as malignant, whereas cells lacking evidence from both criteria were classified as non-malignant. B cells across samples were also integrated using Harmony and subjected to Leiden clustering. Clusters characterized by proliferation-associated markers (e.g., *MKI67* and *TOP2A*) or PC-associated markers (e.g., *SDC1*, *MZB1*, and *XBP1*) were annotated as PB cells and PCs, respectively. Clusters lacking a sufficiently distinct or consistent transcriptional program were retained as UB cells. Among the remaining B-cell populations, cells were assigned as QMB or nmB cells according to their malignant versus non-malignant classification described above. These integrated annotations were further confirmed by careful review of the DEGs of each B-cell subset and used as the final B-cell identities for downstream analyses.

*RNA velocity analysis*

RNA velocity analysis was performed on macrophage subsets identified from the integrated snRNA-seq dataset. Spliced and unspliced transcript counts were generated using Velocyto (v0.17) by applying the run10x function to Cell Ranger outputs. The resulting loom files were integrated with the Seurat object and converted to an h5ad format. RNA velocity was estimated using scVelo (v0.2.4) in Python (v3.6). Following preprocessing, including filtering, normalization, selection of highly variable genes, and calculation of first- and second-order moments based on nearest-neighbor graphs using the scv.pp.filter_and_normalize and scv.pp.moments functions, RNA velocities were computed using the dynamical model

implemented in the scv.tl.velocity function. Velocity fields were projected onto the UMAP embedding and visualized using the scv.pl.velocity_embedding_stream function.

*Trajectory and pseudotime analysis*

Trajectory analysis was performed on macrophage subsets identified from the integrated snRNA-seq dataset using Monocle3 (v1.4.26). A cell_data_set object was generated directly from the Seurat object using the as.cell_data_set function while retaining the existing UMAP embedding and cell annotations. A principal graph was learned on the UMAP manifold using the learn_graph function with partitions disabled (use_partition = FALSE), and pseudotime was calculated using the order_cells function. Based on both RNA velocity analysis and the biological characteristics of the TRL2 subset, which exhibited features of homeostatic tissue-resident macrophages, TRL2 macrophages were designated as the root population for pseudotime ordering. The resulting trajectory was used to infer macrophage state transitions and differentiation dynamics.

*Cross-tissue macrophage comparison using MoMacVERSE*

To compare FL macrophage states with macrophages across human tissues, we used the MoMacVERSE reference atlas[25], a publicly available single-cell RNA-sequencing resource comprising macrophages and monocytes from 13 tissues across 41 datasets integrated into a unified transcriptomic framework. The processed Seurat object provided by the authors, containing the gene-expression matrix, cluster annotations, and original UMAP coordinates, was downloaded. Cluster-specific differentially expressed genes were re-evaluated to confirm macrophage subset annotations. Based on the expression of canonical lineage markers and transcriptomic quality metrics, clusters representing doublets or mitochondrial gene-enriched low-quality cells were reannotated accordingly and excluded from downstream cross-tissue macrophage analyses. To evaluate the correspondence between FL macrophage states and cross-tissue macrophage populations, the top 100 DEGs defining each FL macrophage subset were used as subset-specific gene signatures. Signature enrichment was quantified in individual MoMacVERSE cells using Seurat's AddModuleScore function and summarized across MoMacVERSE macrophage clusters. The specificity of each FL macrophage signature for individual MoMacVERSE clusters was quantified using the Kruskal–Wallis effect size ($\eta^2[H]$). To assess global transcriptional similarity between FL and MoMacVERSE macrophage states, cluster-level average expression profiles were generated using the union of the top DEGs from both datasets. Gene expression was standardized within each dataset, and pairwise Pearson correlations were calculated between FL and MoMacVERSE macrophage clusters. To further quantify the correspondence between FL macrophage states and MoMacVERSE macrophage subsets, receiver operating characteristic analysis was performed using FL macrophage signature scores in individual

MoMacVERSE cells. For each FL-derived signature, the area under the curve was calculated for each MoMacVERSE macrophage subset relative to all other subsets, providing a quantitative measure of how strongly each FL macrophage program corresponded to an individual MoMacVERSE macrophage subset.

**Processing of TMA blocks**

FFPE TMA blocks were sectioned at 5 µm thickness using a microtome. For each TMA, one H&E-stained section and two unstained sections were prepared. H&E slides were digitally scanned and reviewed at MD Anderson Cancer Center. Unstained sections were allowed to dry overnight before shipment to MD Anderson Cancer Center by overnight courier service.

**Spatial molecular imaging (SMI)**

Spatial molecular imaging was performed at MD Anderson Cancer Center using the CosMx SMI platform (Bruker Spatial Biology). Sample preparation was performed according to the CosMx SMI Slide Preparation for RNA Assays User Manual (MAN-10184, Bruker Spatial Biology). FFPE tissue blocks were sectioned to 5 µm slices using a microtome. The sample processing, staining, imaging, and cell segmentation were performed according to the manufacturer's protocol (MAN-10184, Bruker Spatial Biology). Briefly, tissue sections were placed on VWR Superfrost Plus Micro Slides (Cat# 48311-703) for optimal adherence. Slides were then dried at 60 °C overnight, followed by deparaffinization using Xylene (5 min) and Ethanol (5 min). Subsequently, the slides were placed in pre-heated target retrieval buffer and incubated at 100 °C for 15 min. The slides were treated with proteinase K (3 µg/mL) for digestion at 40 °C for 30 min. The slides were subjected to fiducial treatment for 5 min and were post-fixed by 10% neutral-buffered formalin (EMS Diasum: 15740). Fixation was stopped using stopping buffer (Tris Glycine Buffer (0.1M)) and subsequently blocked using N-hydroxysuccinimidyl acetate (Fisher Scientific, 26777) and washed with Saline-Sodium Citrate buffer (Invitrogen: AM9763). 1 nM RNA-ISH probes (CosMx Human 6K Discovery Panel) were applied for hybridization at 37°C overnight. After a stringent wash with 50% Deionized formamide (ThermoFisher AM9342), the slides were stained with morphology markers (pan-cytokeratin, CD68, CD298/B2M, CD45, and DAPI) for visualization and cell segmentation. A flow cell was assembled on top of the slide and loaded onto the CosMx SMI system (SMI Serial Number: INS2304H0071 & INS2311H0265) for UV bleaching, imaging acquisition, cycling processing, and scanning according to the Instrument User Manual (MAN-10161-05, Bruker Spatial Biology).

## SMI data analysis

*SMI data preprocessing*

Raw CosMx SMI data were processed using AtoMx (Bruker Spatial Biology), a cloud-based spatial informatics platform, for transcript decoding and cell segmentation. Detected probes were classified as target transcripts, negative control probes consisting of synthetic sequences not expected to hybridize to endogenous RNA, or system control probes representing non-decodable barcode combinations. Cell segmentation was performed using DAPI nuclear staining, membrane morphology markers, and pretrained Cellpose deep-learning models to identify individual cells and delineate cell boundaries[50]. Decoded transcripts and negative control probes were assigned to segmented cells, generating cell-by-gene expression matrices, cell-level metadata, transcript coordinates, cell boundary polygons, cell centroid coordinates, and field-of-view annotations. Downstream quality control, normalization, dimensionality reduction, visualization, and differential gene expression analyses were performed using Seurat (v5.1.0).

*QC*

QC was performed at both the sample and cell levels. At the sample level, we carefully evaluated the spatial integrity of all samples, as preservation of the macroscopic spatial architecture is critical for spatial analyses of FL, and specimens with collapsed spatial structures were removed. Among the two cores from the same sample in the LEO cohort with well-maintained spatial structures, the core with the higher median number of features per cell was selected for QC and downstream analyses, thereby generating a high-quality core dataset. Samples with the median number of features of less than 100 were removed as low-quality samples. Cells were filtered to retain those with nCount_RNA > 0, nFeature_RNA below three times the median, and above the 10th percentile of the nFeature_RNA distribution. Cells were further excluded if they showed high background signal, defined as nFeature_negprobes ≥ 10, nCount_negprobes ≥ 10, nFeature_falsecode ≥ 10, or nCount_falsecode ≥ 30. We subsequently performed sample-level unsupervised clustering analysis to identify B cell subsets, as described in the “Sample-level clustering analysis to annotate B cell subsets” section below. Samples without any detectable B cell clusters were further removed.

*Sample-level clustering analysis to annotate B cell subsets*

After sample-level quality control, single-cell transcriptome data for each sample were normalized using the NormalizeData function. Data were then scaled using the ScaleData function and subjected to principal component analysis using the RunPCA function. Based on the principal components, a shared nearest neighbor graph was constructed, followed

by unsupervised clustering using the FindNeighbors and FindClusters functions (dimensions = 50, resolution = 0.6–2.5). Clustering results were visualized using UMAP (the RunUMAP and DimPlot functions). DEG analysis was performed using the FindMarkers or FindAllMarkers functions of the Seurat package as appropriate. The DEGs were filtered to extract those expressed in at least 10% of cluster cells with an expression log2 fold change > 0.25 and an adjusted *P* value (based on the Bonferroni correction) of <0.05. The listed DEGs were used for the annotation of cell clusters by carefully reviewing the expression of canonical markers along with an extensive literature search. B-cell clusters were identified based on the expression of canonical B-cell markers (e.g., *MS4A1*, *CD19*, *CD79A*, and *CD79B*) and PC markers (e.g., *MZB1*, *XBP1*, *SDC1*, and *JCHAIN*), together with the absence of canonical markers of other lineages, including T/NK (e.g., *CD3D* and *GNLY*), myeloid (e.g., *CD68*), and endothelial/stromal cells (e.g., *PECAM1* and *ACTA2*). Samples without detectable B-cell clusters were excluded. Clusters annotated as other lineages, such as red blood cells and epithelial cells, were removed. Malignant B-cell populations were distinguished from non-malignant B-cell populations based on immunoglobulin light chain restriction, as described in previous studies[13,14,51]. Specifically, expression of *IGKC* (kappa) and *IGLC1/2* (lambda) was projected onto the UMAP for each sample. B-cell clusters exhibiting immunoglobulin light-chain restriction, consisting predominantly of cells expressing either *IGKC* or *IGLC1/2* together with double-negative cells lacking expression of both genes, were annotated as malignant. In contrast, clusters containing a mixture of both kappa- and lambda-expressing cells were annotated as nmB cells. B-cell clusters expressing proliferation markers (e.g., *MKI67*, *STMN1*, and *H3C2*) were annotated as PB cells, while other malignant B-cell clusters were annotated as QMB cells. PCs were annotated based on the expression of PC markers described above. As an additional quality-control step, the spatial distributions of PB, QMB, and nmB clusters were examined in each sample to confirm consistency with expected biological localization patterns, including preferential localization of PB and QMB cells within follicles and nmB cells in extrafollicular regions. Finally, cells identified as B-cell subsets by sample-level clustering, those that were also classified as B cells by supervised lineage separation, as described in the "Supervised LME cell typing by co-embedding SMI and snRNA-seq data, Step 2" section, were considered confidently annotated B-cell subsets and used for downstream analyses. B cells identified by supervised lineage separation but not included in B cell clusters in sample-level clustering were annotated as UB cells.

*Supervised LME cell typing by co-embedding SMI and snRNA-seq data*

To improve cell-type annotation of CosMx SMI data, we implemented a hierarchical supervised cell-typing framework using a reference snRNA-seq dataset. Compared with snRNA-seq, CosMx SMI measures a restricted set of transcripts from thin tissue sections

and therefore typically captures fewer transcripts per cell. In addition, transcript assignment may be affected by segmentation inaccuracies in densely packed tissues. These factors reduce separation of cellular populations in expression space and limit the accuracy of cell-type annotation based on SMI data alone. To address these limitations, SMI and snRNA-seq datasets were integrated into a shared embedding space, enabling supervised classification of SMI cells using the reference snRNA-seq annotations. For supervised annotation, the reference snRNA-seq dataset was restricted to the 6,175 genes included in the CosMx Human 6K Discovery Panel. SMI cells corresponding to lineages absent from the snRNA-seq reference were excluded based on sample-level clustering analyses (see "Sample-level clustering analysis to annotate B cell subsets"). Cell identities were assigned hierarchically through four sequential steps: (1) initial label assignment, (2) major lineage classification, (3) cell-type classification within each lineage, and (4) cell-subset classification within each cell type. To accommodate approximately four million SMI cells, cells were randomly shuffled and partitioned into subsets containing at most 200,000 cells at each classification stage. Annotation was performed independently for each subset, after which cells were pooled before proceeding to the next classification level. The analyses described below were performed primarily using Seurat (v5.1.0) in R (v4.3.3 or v4.5.1).

Step 1: Initial label assignment.

An initial set of cell-type labels was assigned to SMI cells using a custom reference generated from the snRNA-seq dataset. Mean expression profiles were calculated for pseudobulk populations containing more than 100 cells and used to construct a custom celldex reference for SingleR-based prediction. Predicted labels were subsequently refined using a k-nearest-neighbor approach in PCA space (k = 50). Cells were considered high-confidence if at least 75% of neighboring cells shared the same predicted label. These high-confidence SMI annotations were retained and combined with the snRNA-seq labels for subsequent supervised classification.

Step 2: Major lineage classification.

Major lineage assignment was performed by integrating SMI and snRNA-seq datasets into a common embedding space followed by supervised classification. To emphasize lineage-specific biological variation while reducing technology-associated batch effects, analyses were restricted to marker genes identified from the snRNA-seq dataset. For each cell type, the top 100 DEGs (adjusted $P < 0.05$ and fold change > 1.5) were selected. Both datasets were processed using Seurat functions including SCTransform, PrepSCTIntegration, and RunPCA. Integration anchors were identified from the top 50 principal components using the FindIntegrationAnchors function with reciprocal PCA (RPCA), followed by data integration using the IntegrateData function. RPCA was chosen because it reduces overcorrection while

preserving biological variation associated with malignant populations. A random forest classifier (500 trees) was trained using the top 50 integrated PCs together with reference labels derived from the snRNA-seq dataset and the high-confidence SMI annotations obtained in Step 1. Incorporation of high-confidence SMI cells allowed the model to capture SMI-specific technical characteristics that were not represented in the snRNA-seq data. Predicted labels were subsequently grouped into four major lineages: B cells, non-B lymphoid cells, myeloid cells, and non-hematopoietic cells (NHCs). B cells were subsequently assigned to B-cell subsets by integrating the B-cell lineage annotations generated in this framework with the results of the sample-level clustering analysis.

Step 3: Cell type classification within lineages.

Following lineage assignment, each lineage was analyzed independently to resolve finer cell identities. Non-B lymphoid cells were classified into CD4 T cells, CD8 T cells, and natural killer/natural killer T/innate lymphoid cell (NK/NKT/ILC) cells. Myeloid cells were classified into macrophages, monocytes, dendritic cells (DCs), and plasmacytoid DCs (pDCs), whereas NHCs were classified into blood (BEC) and lymphatic (LEC) endothelial cells and non-endothelial stromal cells (NESCs). For each lineage, the top 100 DEGs for each cell type relative to all other cell types within the same lineage were selected as features. SMI and snRNA-seq datasets were integrated using canonical correlation analysis (CCA) in Seurat. Both datasets underwent SCTransform normalization, PrepSCTIntegration, and RunPCA before anchor identification. Unlike the RPCA-based strategy used for lineage classification, CCA was applied because malignant populations had already been excluded, allowing more effective alignment of shared microenvironmental cell populations. The RunHarmony function in Harmony (v1.2.4) was applied to the snRNA-seq dataset to correct sample-specific batch effects, and the resulting embedding was used to construct a reference UMAP model. Transfer anchors were identified using the FindTransferAnchors function, and cell-type labels together with UMAP coordinates were transferred to SMI cells using the MapQuery function.

Step 4: Cell subset classification.

The final stage of annotation resolved transcriptionally distinct cell subsets within each cell type. For each cell type, marker genes were selected by identifying the top 100 DEGs for each subsets relative to all remaining subsets. SMI and snRNA-seq datasets were integrated using the same CCA-based framework described above, and subset identities together with UMAP coordinates were assigned to SMI cells through reference mapping using the FindTransferAnchors and MapQuery functions.

*Follicle detection and cell-cell distance measurement*

For each sample, the single-cell gene expression matrix, spatial information, and cell type classification data were transformed into a SpatialExperiment object using the SPIAT package (v1.11.0). In FL samples, neoplastic follicular regions were identified using a spatial graph–based approach implemented in R package imcRtools (v1.15.0). Briefly, a cell–cell spatial neighbor graph was constructed for each sample from cell centroid coordinates using the buildSpatialGraph function (expansion model), with edges defined between cells located within 15 μm. Cells annotated as PB or QMB cells in FL samples and PB and nmB cells in tonsil samples were used to identify spatially connected aggregates using the patchDetection function (minimum patch size = 10 cells, expand_by = 10 μm), which were defined as intrafollicular regions, whereas all remaining cells were classified as extrafollicular. Follicular regions were identified in all samples. In addition, the Euclidean distance from each cell to the nearest intrafollicular cell (defined by patch_id) was computed for all cells within each sample using the minDistToCells function and referred to as the minimal distance to follicle.

*Identification of cellular neighborhoods and spatial niches*

Cellular neighborhoods were defined using a k-nearest neighbor graph–based approach implemented in imcRtools. Briefly, a spatial graph was constructed across all cells using the buildSpatialGraph function with the k-nearest neighbor setting (k = 20) based on cell centroid coordinates. For each cell, the cellular composition of its local neighborhood was quantified using the aggregateNeighbors function, generating a neighborhood composition matrix based on annotated cell phenotypes. Spatial niches were then defined by grouping cells with similar neighborhood compositions using k-means clustering of this matrix. To determine the optimal number of clusters, k-means clustering was performed across a range of cluster numbers (centers = 3–30), and the results were evaluated using elbow plots together with careful manual inspection for the emergence of distinct new niches and redundancy between niches. Based on these assessments, 10 spatial niches were selected for downstream analyses. DEG analysis across spatial niches was performed as described in the “Sample-level clustering analysis to annotate B cell subsets” section, treating cells belonging to each niche as a single cluster.

*Cell subset-specific spatial enrichment analysis*

To assess the enrichment of LME cell subsets around specific malignant B-cell states identified in spatial niche analysis and to evaluate reciprocal interactions, cell subset-specific spatial enrichment analysis was performed within intrafollicular regions. Cell subsets were restricted to those with high intrafollicular representation (top 50% based on intrafollicular proportion). For each cell subset of interest, neighboring cells were identified using the k-nearest neighbor graph (k = 20), and the composition of neighboring cell types

was quantified as counts of neighboring cells. As a background reference, the overall cell subset composition within intrafollicular regions was used. For analyses centered on malignant B-cell states (PB and QMB), malignant B-cell populations were excluded from both neighbor counts and background proportions to focus on LME interactions and avoid self-enrichment effects. For reciprocal analyses centered on macrophage subsets, only the corresponding center cell subset was excluded, while malignant B-cell populations were retained. For each cell type, observed neighbor counts were compared with expected counts based on background proportions using a binomial test. *P* values were adjusted for multiple testing using the Benjamini–Hochberg method. Enrichment or depletion was defined based on the direction of change in observed proportions relative to background, and effect sizes were quantified as log2 fold change of neighbor proportions compared to background.

*Identification of intrafollicular FL archetypes of microenvironment (FLAMEs)*

To identify archetypal patterns of the intrafollicular microenvironment, non-negative matrix factorization (NMF) was applied to cell subset composition profiles within spatially defined intrafollicular regions. Cell subsets were limited to top 50% LME subsets with shorter distances to follicle. Multiple thresholds were evaluated to minimize inclusion of extrafollicular cell subsets while retaining intrafollicular cell subsets, and a threshold of 50% was selected. A sample-by-cell-subset composition matrix was constructed using intrafollicular cell counts. Samples with fewer than 100 non-B cells or fewer than 10 detected non-B cell subsets were excluded. Cell counts were then converted to intrafollicular cell proportions for each sample and used for NMF. NMF was performed using the R package NMF (v0.28) to decompose the composition matrix into latent factors representing cellular modules and FLAMEs. To determine the optimal factorization rank, an NMF rank survey was conducted across candidate ranks, and multiple metrics, including silhouette scores, were evaluated, resulting in the selection of rank = 5. For each rank, NMF was repeated 100 times to ensure robustness, and a consensus matrix was generated. Samples were assigned to FLAMEs based on consensus clustering, and five FLAMEs were retained without further aggregation. FLAMEs were annotated based on the dominant cell subsets and combinations of cellular modules characterizing each FLAME.

*Cell size analysis*

Cell size was assessed using cell area measurements derived from the default cell segmentation output of the CosMx SMI platform. Cell area values were used directly without additional segmentation or morphological processing. As a quality check, relative cell area differences across major cell populations were confirmed to be consistent with expected cellular morphology, including smaller lymphoid cells compared with myeloid cells and

NHCs, larger PB and QMB cells compared with nmB cells, and larger PB cells compared with QMB cells.

*Proliferation gene signature analysis*

A proliferation gene signature was defined using the top 100 DEGs with the highest average log2 fold change characterizing PB cells. CosMx SMI raw count data were normalized using Seurat LogNormalize and proliferation signature scores were calculated using AddModuleScore with 100 control genes. For analyses across FLAMEs, proliferation signature scores were evaluated in PB and QMB cells, and the median score was calculated for each sample and compared across FLAMEs.

**Multiplex spatial protein imaging (SPI) analysis**

*SPI data processing*

We analyzed multiplex SPI data of 242 newly diagnosed FL samples from a previously published study[12]. All samples included in this protein imaging dataset were independent of the CosMx SMI cohort and were linked to clinical data, which were partially updated for the present study. The single-cell protein expression matrix and centroid coordinate data generated in the original study were used directly for the present analysis. Cell centroid coordinates and fluorescence intensities were extracted and converted into a Seurat object. Data were normalized using the NormalizeData function, scaled using the ScaleData function, and subjected to principal component analysis using RunPCA. Batch effects were corrected using the RunHarmony function (from Harmony). After integration, unsupervised clustering was performed using FindNeighbors and FindClusters, and visualized by UMAP using the RunUMAP and DimPlot functions. Clusters were annotated based on canonical marker expression identified by differential expression analysis. The integrated Seurat object was converted into a SpatialExperiment object, and spatial compartmentalization analysis using proliferating and quiescent B cells, as well as calculation of minimal distances to follicles, were performed using the same methods as those applied in the CosMx SMI analysis. In addition, SPI was performed on the CosMx SMI cohort using the CODEX platform according to the manufacturer's instructions and using similar methods to those applied to the independent cohort[12], with a panel including CD20 (Akoya, 232175), CD68 (Akoya, 232176), CD21 (Akoya, 240003), PD-1 (Akoya, 240035), CD3e (Akoya, 240006), CD8 (Akoya, 232151), BCL2 (abcam, ab182858), and Ki67 (Akoya, 232179). These data were used for orthogonal visualization of representative protein expression patterns corresponding to the spatial FLAMEs identified by CosMx SMI analysis.

*Quantification of intrafollicular percentage of macrophages (IFMP)*

In SPI data, identification of some cell populations contributing to FLAMEs was challenging or not directly comparable to that in the CosMx SMI dataset. For example, FDCs, represented by CD21 positivity, exhibit large cell bodies and highly dendritic morphologies that form extensive contacts with surrounding B cells. Consequently, SPI signals frequently reflect mixed protein expression from neighboring cells, resulting in overestimation of CD21-positive cells and substantially different FDC abundances compared with those observed in CosMx SMI data. In addition, nmB cells could not be reliably distinguished from malignant B-cell populations because markers enabling their separation were not available in the SPI panel. In contrast, macrophages were robustly identified as a CD68-positive cell cluster in SPI data. Therefore, we sought to develop a simplified metric to predict the FM-FLAME based on intrafollicular macrophage enrichment. To define this metric, we first calculated the intrafollicular percentage of macrophages (IFMP) in the CosMx SMI dataset using two approaches: (1) all macrophage subsets and (2) only macrophage subsets included in the FLAME analysis (C1, C2, C4, C5, and C7). The predictive performance of each approach for identifying the FM-FLAME was evaluated using receiver operating characteristic analysis. Both approaches demonstrated comparable predictive performance, although the all-macrophage approach yielded a slightly higher area under the curve. Considering its broader applicability, the all-macrophage approach was selected for subsequent analyses and used to define IFMP. The optimal cutoff for predicting the FM-FLAME was determined using the Youden index, which identified a threshold of 2.41%. For simplicity, the cutoff was rounded to 2.5%. In SPI data, IFMP was calculated as the proportion of CD68-positive macrophages among all intrafollicular cells, where macrophages were defined by the clustering analysis described above (see “SPI data processing”).

## Cell-cell communication analyses

*Prioritization of ligands that regulate target genes*

NicheNet (nichenetr v2.2.1.1) was used to identify ligands predicted to regulate transcriptional programs in FM1 and PB cells, which were specified as receiver cell populations. NicheNet integrates DEGs for each receiver cell subset with prior knowledge of signaling pathways and gene regulatory networks to prioritize ligands expressed in sender cells. To identify ligands associated with follicular macrophage phenotypes, DEGs for FM1 that were consistently identified in both snRNA-seq and CosMx SMI datasets were used as the input gene set. Cell subsets significantly enriched in the FM1 neighborhood, as identified in the “Cell subset-specific spatial enrichment analysis” described above, were selected as sender cell populations. To identify ligands that specifically induce proliferation in PB cells in the FM-FLAME, DEGs upregulated in PB cells from FM-FLAME samples compared with

non-FM-FLAME samples were used as the input gene set. To investigate the effects of macrophage populations associated with the FM-FLAME on PB cells, macrophage subsets contributing to the FM-FLAME were selected as sender cell populations. Candidate ligands were required to be expressed in more than 10% of cells in at least one sender cell subset. Ligands were ranked according to their ligand activity scores, quantified as the area under the precision–recall curve for prediction of the receiver gene set.

*Cell-cell interactions*

CellPhoneDB (v5.0.0) was used to identify ligand-receptor interactions between FM1 or PB cells and the corresponding sender cell subsets used in the NicheNet analyses above. Gene expression count matrices and cell subset annotations were provided as input, with genes specified using HGNC symbols. Cells were subsampled to include up to 1,000 cells per cell subset to avoid imbalances in cell numbers. CellPhoneDB statistical analysis was performed using 1,000 permutations, and ligand-receptor interactions were evaluated when the interacting genes were expressed in at least 10% of cells within the corresponding cell subset. Significant ligand-receptor interactions were defined by a $P$ value < 0.05.

*Combining NicheNet and CellPhoneDB analyses*

NicheNet and CellPhoneDB analyses were performed independently using both snRNA-seq and CosMx SMI datasets to identify reproducible interactions across the two datasets. To mitigate the sparsity of CosMx SMI data, we restricted the SMI data analysis to the top 20% of high-quality cells ranked by the number of detected features per cell. In analyses focusing on cell-cell communications involving PB cells and macrophage subsets, CosMx SMI data were restricted to cells within CN1 (PB/FM niche). Only ligands and interactions identified in both snRNA-seq and CosMx SMI datasets were retained. Ligands prioritized by NicheNet and supported by significant CellPhoneDB interactions were selected for downstream visualization and interpretation.

**Enzyme-Linked Immunosorbent Assay (ELISA)**

To validate the cell-cell communication analysis implicating CD40L in the induction of the FM1 phenotype, we performed ELISA using U937 cells, a human monocytic cell line. The U937 cells were pretreated with 200 ng/mL PMA (Sigma, P8139-1MG) to induce differentiation, followed by incubation with 100 ng/mL CD40L (R&D Systems, 6420-CLB). The supernatant medium was subjected to ELISA-based quantification of APRIL concentrations according to the manufacturer's instructions (Invitrogen, BMS2008). Briefly, the supernatant from the CD40L-stimulated cells was added to the antibody-coated microwells and co-incubated with biotin-conjugate for 2 hr. The wells were washed

thoroughly and incubated with streptavidin-HRP for 1 hr. Subsequently, the HRP substrate was added to the wells. The reaction was terminated by the addition of stopping solution and absorbance was measured at 450 nm using a Tecan Infinite 200 PRO plate reader. A standard curve was prepared from seven human APRIL standard dilutions and APRIL concentrations in the samples were determined.

**Whole-exome sequencing (WES)**

Genomic DNA was extracted from nuclei samples using the AllPrep DNA/RNA Kit (Qiagen). DNA quality and quantity were assessed using the Agilent 4200 TapeStation (Agilent Technologies) and Qubit (Invitrogen). Exome libraries were prepared using the SureSelect Human All Exon v7 kit (Agilent Technologies) according to the manufacturer's protocol. Libraries were sequenced on an Illumina NovaSeq 6000 using a PE100 S4 flow cell and a 200-cycle v1.5 kit, targeting 100 million total reads per sample (approximately 100× coverage).

**WES data preprocessing**

*Raw data processing and quality control*

Raw paired-end FASTQ files were initially assessed for sequencing quality using FastQC (v0.11.9). Adapter sequences and low-quality bases were removed using Trimmomatic (v0.39) in paired-end mode. Following trimming, a second round of quality assessment was performed using FastQC to verify the removal of adapter contamination and assess overall read quality. Only high-quality paired reads were retained for downstream processing. Trimmed reads were aligned to the GRCh38.p14 reference genome using BWA-MEM (v0.7.19). Resulting SAM files were converted to coordinate-sorted BAM files and indexed using SAMtools (v1.16.1). Alignment quality metrics were evaluated using Qualimap (v2.2.2d) to assess sequencing coverage, mapping quality, insert size distribution, and duplication rates. Read group information was added using Picard (v2.27.4), assigning sample-specific identifiers and Illumina sequencing platform metadata. PCR and optical duplicates were subsequently identified and marked using GATK (v4.6.2.0) MarkDuplicates. Duplicate-marked BAM files were sorted and indexed using SAMtools.

Exome capture performance was evaluated using GATK CollectHsMetrics. Target regions corresponded to the Agilent SureSelect Human All Exon V7 capture design (S31285117). Capture intervals were converted from BED format to Picard interval list format using GATK BedToIntervalList and used as bait and target intervals during hybrid-selection metric

collection. Base quality score recalibration (BQSR) was performed using GATK. Recalibration tables were generated using GATK BaseRecalibrator with known variant resources from dbSNP build 138 and the Mills and 1000 Genomes gold-standard indel dataset for GRCh38. Recalibration was restricted to exome target intervals. Corrected base quality scores were then applied using GATK ApplyBQSR to generate final analysis-ready BAM files. Recalibrated BAM files were indexed using SAMtools for downstream somatic variant calling.

*Somatic variant calling and annotation*

Somatic single-nucleotide variants (SNVs) and small insertions/deletions (indels) were identified using GATK Mutect2 (v4.6.2.0) in matched tumor–normal mode. Analysis-ready BAM files generated following base quality score recalibration were used as input. For each patient, tumor and matched normal samples were jointly analyzed against the GRCh38.p14 reference genome. Variant calling was restricted to the Agilent SureSelect Human All Exon V7 target regions using the corresponding interval-list file. Matched normal samples were incorporated to facilitate discrimination of somatic mutations from germline variation and sequencing artifacts. Candidate somatic variants were filtered using GATK FilterMutectCalls according to GATK Best Practices.

Somatic variants were functionally annotated using SnpEff (v5.2f) with a custom GRCh38/hg38 annotation database. Variant annotations included predicted functional consequences, such as synonymous, missense, nonsense, splice-site, frameshift, and in-frame insertion/deletion variants, as well as affected genes, transcripts, coding sequences, and protein changes. Annotated variant call format (VCF) files were used for downstream analyses and interpretation of somatic mutations.

*Identification of tumor-enriched variants using HaplotypeCaller*

To provide an orthogonal assessment of tumor-associated variants, variant calling was performed independently on tumor and matched normal samples using GATK HaplotypeCaller (v4.6.2.0). Analysis-ready BAM files generated following base quality score recalibration (BQSR) were used as input, and variant discovery was restricted to the Agilent SureSelect Human All Exon V7 target regions. Variants were called relative to the GRCh38.p14 reference genome and exported in VCF format. Resulting VCF files were normalized using BCFtools (v1.22.1) against the GRCh38.p14 reference genome to ensure consistent representation of multiallelic variants and indels. Variants unique to the tumor sample were identified by subtracting variants detected in the matched normal sample using BCFtools isec. Variants present exclusively in the tumor sample were retained as tumor-enriched variants for downstream analyses. The resulting VCF files were indexed and

summarized using BCFtools statistics, including total variant counts, single-nucleotide variant (SNV) counts, indel counts, and transition-to-transversion ratios.

*Consensus variant calling*

To generate a high-confidence variant set, somatic variants identified by Mutect2 were intersected with tumor-enriched variants identified from the HaplotypeCaller-based analysis. Consensus variants were defined as variants detected by both approaches and were identified using bcftools isec, requiring support from both callsets. The resulting consensus set was used for downstream analyses.

*Tumor-only variant calling and consensus identification*

For the Mater cohort, variants were identified from tumor-only WES data using GATK Mutect2 (v4.5.0.0) and HaplotypeCaller (v4.6.2.0). Both callers were applied independently to tumor BAM files using the GRCh38.p14 reference genome, with variant discovery restricted to the Agilent SureSelect Human All Exon V7 target regions. Mutect2 was performed in tumor-only mode to identify candidate somatic single-nucleotide variants (SNVs) and small insertions/deletions (indels), whereas HaplotypeCaller was used for independent variant detection. Functional annotation was performed as described in the "Somatic variant calling and annotation" section. To generate a consensus variant set, variants identified by both callers were intersected using BCFtools isec (v1.22.1), retaining shared variants and preserving SnpEff annotations. The resulting tumor-only consensus variants were used for downstream analyses.

*Consensus variant filtering and downstream analysis*

For the Mater cohort, consensus variants were further filtered to minimize potential germline variants and sequencing artifacts. Variants present in a panel of normals (PoN) were excluded using BCFtools isec (v1.22.1). The remaining variants were annotated with population allele frequencies from the gnomAD database (GRCh38/hg38) using BCFtools annotate. Stringent filtering criteria were applied to retain variants with a maximum gnomAD allele frequency below 0.01, sequencing depth (DP) ≥10 and Mutect2 tumor log-odds score (TLOD) ≥6, when available. The resulting filtered consensus VCF files were converted into mutation annotation format (MAF) files for downstream analyses, including mutation frequency assessment, characterization of recurrently mutated genes and visualization of the mutational landscape using oncoplots.

*Copy number variation analysis*

Copy number alterations (CNAs) were assessed from WES data using CopywriteR. Copy number profiles were generated from aligned, duplicate-marked and sorted tumor BAM files

using the GRCh38/hg38 reference genome, with non-overlapping genomic bins of 250 kb for the LEO cohort and 500 kb for the MATER cohort. For both cohorts, tumor BAM files were supplied as both sample and control inputs to CopywriteR. Genome-wide copy number profiles were generated and visualized using the CopywriteR and plotCNA functions, respectively, for downstream characterization of copy number alterations.

**Clinical association analyses**

EFS was defined as time from date of diagnosis to date of first event, with an event defined as relapse (recurrence of disease after achievement of a complete remission), disease progression (in those patients who were managed by active surveillance and those who were treated and had stable disease or a partial remission), re-treatment (e.g., initiation of 2nd line therapy), transformation to a different lymphoma subset, and/or death from any cause. Associations between CN abundance and EFS were evaluated using Cox proportional hazards regression models, with abundance treated as a continuous variable. Associations between FLAMEs or IFMP category and EFS were evaluated using the Kaplan–Meier method and log-rank tests with survival package (v3.8.3) and visualized using the survminer package (v0.5.1). Associations with clinical characteristics, including the FLIPI risk categories, factors for the FLIPI and GELF criteria, histologic grades, and treatment approaches, were also evaluated when available.

**Statistics and reproducibility**

Statistical analyses were performed using R (v4.5.1). Continuous variables were compared using the Wilcoxon rank-sum test or Kruskal–Wallis test, as appropriate. Associations between categorical variables were evaluated using Pearson's chi-square test of independence or Fisher's exact test, depending on sample size and expected cell frequencies. For contingency table analyses, standardized Pearson residuals were extracted from chi-square test results to identify categories contributing to significant associations. Two-sided p-values were calculated from the standardized residuals under the standard normal approximation and adjusted for multiple testing using the Benjamini–Hochberg procedure. Categories with an FDR-adjusted $P$ value < 0.05 were considered significantly over- or under-represented relative to the expected frequencies under the null hypothesis of independence. Multiple testing correction was performed using the Benjamini–Hochberg method where indicated. Survival curves were estimated using the Kaplan–Meier method and compared using the log-rank test. Cox proportional hazards regression models were

used for survival analyses where indicated. All statistical tests were two-sided, and $P < 0.05$ or FDR < 0.05 was considered statistically significant.

## FIGURE LEGENDS

**Figure 1: snRNA-seq atlas of follicular lymphoma (FL). (A)** Schematic overview of the study design and patient cohorts for snRNA-seq, CosMx spatial molecular imaging (SMI), and multiplex spatial protein imaging (SPI). LN, lymph node. **(B-C)** UMAP projection of all cells analyzed by snRNA-seq and bar plots showing the proportions of cells colored by sample identity (B) and cell types (C). **(D)** UMAP projection of B cells colored by subsets. **(E)** UMAP projection of non-B cell populations, showing subsets identified by unsupervised clustering. Stacked bar plots indicate proportions of each subset in newly diagnosed (ND) or relapsed/refractory (R/R) FL samples. **(F)** Dendrogram of cell subsets following hierarchical clustering of transcriptomic similarity. The background is colored by cell lineages, and the nodes are colored by cell type (top) or subset (bottom). Node size is proportional to the fraction of each cell subset relative to all cells.

**Figure 2: Spatial single-cell atlas of FL. (A)** Circular plot summarizing the composition of the CosMx SMI cohort and associated sample-level annotations. **(B)** Alluvial (left) and stacked bar (right) plots showing the association between histologic grades and treatment approach in patients with FL from the CosMx SMI cohort. Overall differences were assessed using Fisher's exact test. Asterisks indicate significant over- (black) or under- (white) representation based on standardized residuals with Benjamini–Hochberg correction (**FDR < 0.01, ***FDR < 0.001). R-CHOP, rituximab, cyclophosphamide, doxorubicin, vincristine, and prednisone; RB, rituximab-bendamustine; IC, immunochemotherapy; AS, active surveillance. **(C)** Pie charts showing the composition of cell lineages (top) and non-B cell types (bottom) in snRNA-seq (left) and CosMx SMI (right) data. **(D)** Representative spatial distribution of cells colored by cell types. **(E)** Dendrogram of cell subsets following hierarchical clustering of transcriptomic similarity in CosMx SMI data. The background is colored by cell lineages, and the nodes are colored by cell types (top) or cell subsets (bottom). Node size is proportional to the fraction of each cell subset relative to all cells. **(F)** UMAP projection and expression of key markers in cells from a representative FL sample from CosMx SMI data, highlighting B cell subsets identified by sample-level unsupervised clustering. **(G)** Representative spatial distribution of B cell subsets in FL. **(H)** Representative spatial distribution of cells, colored by minimal distance to follicles. **(I)** Sample-level median minimal distances to follicles across cell subsets in FL samples (Kruskal–Wallis test). **(J)** Representative spatial distribution patterns of macrophage subsets relative to follicles.

**Figure 3: Quantitative profiles of spatial cellular niches in FL. (A)** Heatmap showing the composition of cell subsets across cellular niches (CNs) identified in CosMx SMI data. **(B)** Representative hematoxylin and eosin (H&E)-stained tissue section and corresponding CosMx SMI data showing the spatial distribution of cells colored by cell subset, distances to follicles, and CNs (left to right). **(C)** Proportion of each CN across FL and tonsil samples.

**(D)** Pie charts showing the average CN composition by sample type (top) and cohort (bottom). **(E)** Expression of key genes across CNs. **(F)** Representative spatial distribution of CN1 (left) and a magnified view (right) highlighting key cell subsets. Pie chart shows the composition of major cell subsets within CN1. Yellow dashed lines mark follicle boundaries. **(G)** Scatter plot showing log2 ratios of 20-nearest neighbor cell subset proportions around PB and QMB cells relative to background composition in intrafollicular regions. Analyses were restricted to the top 50% of cell subsets ranked by increasing distance to the follicle (**Figure 2I**, red). **(H)** Bar plots showing log2 ratios of 20-nearest neighbor cell subset proportions around macrophage subsets relative to background composition in intrafollicular regions.

**Figure 4: Non-negative matrix factorization of intrafollicular FL Archetype of MicroEnvironment (FLAME). (A)** Pearson correlation matrix of intrafollicular LME cell subset compositions, with modules (FLAMEs) identified by non-negative matrix factorization. **(B)** Pie charts showing the prevalence of FLAMEs in FL (left) and control tonsil (right) samples in CosMx SMI cohort. **(C)** Representative spatial distributions showing intrafollicular enrichment of key cell subsets in each FLAME. Pie charts indicate the composition of key cell subsets in intrafollicular regions. **(D)** Heatmap showing mean cell type proportions within each FLAME. White and black asterisks indicate significant over- and underrepresentation, respectively, compared with all other FLAMEs (Welch's t test with Benjamini–Hochberg correction: *FDR < 0.05, **FDR < 0.01, ***FDR < 0.001). **(E)** Representative multiplex SPI data for each FLAME case shown in **C**, highlighting enrichment of key cell types (red squares). **(F)** Proportion of PB cells among B cells (left) and all cell (right) across FLAMEs. **(G)** Proportion of PB plus QMB cells among all cells across FLAMEs. **(H)** Sample-level median proliferation signature scores of PB and QMB cells across FLAMEs. The proliferation signature consists of top 100 DEGs in PB cells. **(I)** Sample-level median cell areas of PB and QMB cells across FLAMEs. **(J)** Proportion of cells in CN1 (PB/FM niche) among all cells across FLAMEs. Pairwise two-sided Wilcoxon rank-sum test was used in F–J.

**Figure 5: Transcriptional distinctness, differentiation, and cell-cell communications of follicular macrophages. (A)** Bubble plots showing expression of key genes across macrophage subsets in snRNA-seq data. **(B)** UMAP projection of the MoMac-VERSE colored by described cell types (top) and subsets (bottom). Dashed lines outline the macrophage compartment. **(C)** Expression of key functional markers of follicular macrophages (FMs) in the MoMac-VERSE. **(D)** Pearson correlation of pseudobulk expression profiles between FL and MoMac-VERSE macrophage subsets. **(E)** Area under the receiver operating characteristic curve (AUC) of each FL macrophage signature for identifying each MoMac-VERSE macrophage subset versus all remaining subsets (one-versus-rest classification). Dot size is proportional to the AUC. AUC values below 0.5 were truncated to 0.5. **(F)** CXCL13-expressing macrophages (white arrowheads) detected by multiplex SPI in FL (Abe et al. *Cancer Cell*. 2025). Blue, DAPI. CD20 signal is omitted from the merged panel for clarity (left). **(G)** RNA velocity analysis of macrophage subsets in snRNA-seq data. **(H)** Trajectory inference and pseudotime analysis of macrophage subsets using Monocle 3. **(I)** NicheNet

analysis of snRNA-seq data identifying ligands predicted to regulate FMs, prioritized by area under the precision–recall (AUPR) curve, with corresponding expression of ligand-coding genes across sender cell subsets. LME cell subsets enriched around FMs (**Figure 3H**) were analyzed. Dashed lines highlight key interactions that are consistent between snRNA-seq and SMI datasets. **(J)** Circos plot highlighting CD40LG–CD40 and CSF1–CSF1R interactions between sender cell subsets and FMs based on CellPhoneDB analysis of snRNA-seq data. Ribbon widths indicate interaction strength (scaled mean), and sector widths represent the summed interaction strengths for each cell subset. **(K)** Representative spatial distribution of *CD40LG* and *CD40*. Magnified image (right) highlighting proximal TFH cells and FMs expressing *CD40LG* and *CD40*, respectively. **(L)** APRIL (TNFSF13) levels measured by ELISA in conditioned media from U937 cells cultured with or without PMA (200 ng/mL) and/or CD40L stimulation (100 ng/mL) for 120 hours (one-way ANOVA followed by Šídák's multiple comparisons test). Data are presented as mean ± SD. **(M)** NicheNet analysis of snRNA-seq data identifying ligands from key macrophage subsets predicted to regulate phenotype of PB cells in the FM-FLAME compared with non-FM-FLAMEs. Dot plots show expression of ligand-coding genes across sender cell subsets. **(N)** Circos plot highlighting key interactions between sender macrophage subsets and PB cells based on CellPhoneDB analysis of snRNA-seq data. **(O)** Proposed model of cellular ecosystems in FL. CD40L from TFH cells promotes tissue-resident–like macrophages to acquire FM phenotypes, which in turn support proliferative phenotypes of PB cells.

**Figure 6: Clinicopathological associations of macrophage-enriched microenvironment in FL. (A)** Distribution of FLAMEs across histologic grades (left) and distribution of histologic grades across FLAMEs (right). **(B)** Distribution of BCL2 protein expression status across histologic grades (left) and FLAMEs (right). **(C)** Representative multiplex SPI data showing different BCL2 protein status across FL and tonsil samples in the CosMx SMI cohort. **(D)** Distribution of treatment approaches across FLAMEs. IC, immunochemotherapy; AS, active surveillance. **(E)** Distribution of IC regimens across FLAMEs. **(F)** Kaplan–Meier curves of event-free survival (EFS) according to FM or non-FM-FLAME in the overall FL cohort (left), patients treated with IC (center), and patients managed with AS (right). **(G–I)** Proportion of cells in CN1 (PB/FM niche) among all cells stratified by FLIPI risk group (G), histologic grade (H), and treatment approach (I) (two-sided Wilcoxon rank-sum test). **(J)** Forest plots of univariable Cox proportional hazards models for EFS based on sample-level CN proportions in the overall FL cohort (left), patients treated with IC (center), and patients managed with AS (right). CN proportions were analyzed as continuous variables. Circle colors indicate statistical significance (two-sided Wald test). NS, not significant. **(K)** EFS according to CN1 abundance in the overall FL cohort (left), patients treated with IC (center), and patients managed with AS (right). Patients were dichotomized at the median CN1 abundance in the overall cohort. For F and K, two-sided log-rank test was used. For A, B, D, and E, overall differences were assessed using chi-square or Fisher's exact tests. Asterisks indicate significant over- or underrepresentation based on standardized residuals with Benjamini–Hochberg correction (*FDR < 0.05, **FDR < 0.01, ***FDR < 0.001). White and black asterisks indicate over- and underrepresentation, respectively.

**Figure 7: Orthogonal validation of FM-FLAME using intrafollicular macrophage percentage (IFMP) in an independent FL SPI cohort. (A)** Receiver operating characteristic curves of intrafollicular macrophage percentage (IFMP) for predicting the FM-FLAME in CosMx SMI data using all macrophage subsets. AUC, area under the curve. **(B)** Confusion matrix summarizing predictive performance in CosMx SMI data, including sensitivity, specificity, accuracy, and positive (PPV) and negative (NPV) predictive values for FM versus non-FM-FLAMEs based on high (≥2.5%) or low (<2.5%) IFMP. **(C)** Histograms showing the distribution of IFMP in CosMx SMI and multiplex spatial protein imaging (SPI) data. Pie charts show the proportion of high and low IFMP cases. **(D)** Representative spatial distributions of cells in high (left) and low (right) IFMP cases in the SPI FL dataset (Abe et al. *Cancer Cell*. 2025), highlighting intrafollicular PB cells and macrophages. Pie charts indicate intrafollicular cellular composition. **(E)** Representative SPI of high (top) and low (bottom) IFMP cases with histologic grades 3B and 1/2, respectively. **(F)** Distribution of high and low IFMP across histologic grades (left) and the distribution of histologic grades across IFMP groups (right) in the SPI FL dataset. **(G)** Distribution of BCL2 protein expression status across histologic grades (left) and IFMP groups (right). For F and G, overall differences were assessed using chi-square or Fisher's exact tests. Asterisks indicate significant over- or underrepresentation based on standardized residuals with Benjamini–Hochberg correction (*FDR < 0.05, **FDR < 0.01, ***FDR < 0.001). White and black asterisks indicate over- and underrepresentation, respectively. **(H)** EFS according to IFMP in the SPI FL cohort (left), patients treated with IC (center), and patients managed with AS (right) (two-sided log-rank test was used).

**Figure S1: snRNA-seq analysis of FL. (A)** Flow diagram of snRNA-seq cohort selection and quality control. **(B)** Circular plot summarizing the composition of the snRNA-seq cohort and associated sample-level annotations. **(C)** Bubble plot showing expression of key genes across non-B cell types. **(D)** Heatmaps of marker genes for clustering-defined subsets within each non-B cell type. **(E)** UMAP projection of B cells colored by B cell receptor (BCR) sequencing results (left) and inferred copy number variation (CNV) (right). **(F)** Bubble plot showing expression of key genes across B cell subsets. **(G-H)** Proportion of PB cells among all cells across histologic grades (G) and between newly diagnosed (ND) and relapsed/refractory (R/R) FL (H) (pairwise two-sided Wilcoxon rank-sum test).

**Figure S2: CosMx SMI analysis of FL. (A)** Flow diagram of CosMx SMI cohort selection and quality control. **(B)** UMAP projection of non-B cell populations, showing subsets identified by supervised annotation in a representative analytical subgroup. Stacked bar plots indicate proportions of each subset in FL and control tonsil samples. **(C)** Bubble plot showing expression of key genes across non-B cell types. **(D)** Heatmaps of marker genes for subsets within each non-B cell type. **(E)** Box plots showing the log10-transformed ratio of *IGKC*-expressing to *IGLC1/2*-expressing cells across PB, QMB, and nmB populations. FL samples with <10% *IGKC*-expressing and <10% *IGLC1/2*-expressing cells were excluded as lacking detectable light chain expression. Malignant B cell populations were classified as kappa- or lambda-biased based on the ratio (kappa-biased, ≥1.5; lambda-biased, <1.5). *P* values were

calculated using two-sided Wilcoxon rank-sum test with Benjamini–Hochberg correction. **(F)** Bubble plots showing expression of key genes across B cell subsets.

**Figure S3: Consistent gene expression profiles of cell subsets between snRNA-seq and CosMx SMI datasets.** Bubble plots showing expression of key genes across non-B cell subsets in snRNA-seq (left) and CosMx SMI (right) datasets.

**Figure S4: Spatial profiling of cell populations in CosMx SMI. (A)** Spatial distribution of B cell subsets used for follicle detection in FL and tonsil samples. **(B)** Sample-level median minimal distances to follicles across cell subsets in tonsil samples (Kruskal–Wallis test). **(C)** Representative spatial distribution patterns of key cell subsets relative to follicles in FL and tonsil samples. **(D)** Representative spatial distribution patterns of macrophage subsets relative to follicles in FL and tonsil samples.

**Figure S5: Associations of gene mutations with macrophage subset proportions, CNs, and FLAMEs. (A)** Oncoplot showing gene mutations across FL biopsies in the snRNA-seq cohort. **(B)** Dot plots showing ratios of mean macrophage subset proportions in mutant versus wild-type (WT) biopsies in the snRNA-seq cohort. FM, FM_IEG, FM + FM_IEG, and Mac_Cycl proportions were calculated as percentages of all macrophages. Biopsies containing fewer than 10 macrophages were excluded (two-sided Wilcoxon rank-sum tests with Benjamini–Hochberg correction for multiple testing). **(C)** Oncoplot showing gene mutations across FL samples in the CosMx SMI cohort. **(D)** Dot plots showing ratios of mean macrophage subset proportions in mutant versus WT samples in the CosMx SMI cohort. FM, FM_IEG, FM + FM_IEG, and Mac_Cycl proportions were calculated as percentages of all macrophages (two-sided Wilcoxon rank-sum tests with Benjamini–Hochberg correction for multiple testing). **(E)** Dot plots showing associations between gene mutations and CN proportions in the CosMx SMI cohort, expressed as rank-biserial correlations comparing mutant versus WT samples (two-sided Wilcoxon rank-sum tests with Benjamini–Hochberg correction for multiple testing). **(F)** Dot plots showing associations between gene mutations and FLAMEs in the CosMx SMI cohort, expressed as $\log_2$ odds ratios comparing each FLAME with all other FLAMEs (two-sided Fisher's exact tests with Benjamini–Hochberg correction for multiple testing).

**Figure S6: Characterization of macrophage subsets in FL. (A)** Comparison of sample-level median cell areas across macrophage subsets in FL (left) and tonsils (right) (pairwise two-sided Wilcoxon rank-sum test). **(B)** Representative hematoxylin and eosin staining images of FL and tonsil samples. Dashed lines indicate follicular regions. Rectangles in the tonsil samples highlight typical tingible body macrophages. **(C)** Expression of key markers for each macrophage subset in the MoMac-VERSE. **(D)** Expression of the top 10 DEGs for FMs in the MoMac-VERSE. **(E)** Enrichment of the top 100 DEG signatures for each FL macrophage subset across macrophage subsets in the MoMac-VERSE. **(F)** UMAP projection of cells from the SPI data (Abe et al. *Cancer Cell*. 2025), colored by cell types. QB, quiescent B. **(G)** Expression of key protein markers used for cell type classification in SPI data. **(H)** UMAP projection showing subclustering of macrophages from SPI data. **(I)** Expression of key

protein markers used for macrophage subset classification in SPI data. **(J)** Sample-level median minimal distances to follicles across macrophage subsets in SPI data (pairwise two-sided Wilcoxon rank-sum test).

**Figure S7: Cell-cell communication analysis of follicular macrophages and PB cells. (A)** NicheNet analysis of CosMx SMI data identifying ligands predicted to regulate FMs, prioritized by area under the precision–recall (AUPR) curve, with corresponding expression of ligand-coding genes across sender cell subsets. **(B-C)** Bubble plots summarizing significantly enriched ligand–receptor interactions targeting FMs mediated by LME subsets significantly enriched around FMs (**Fig. 3H**) in snRNA-seq (B) and CosMx SMI data (C). **(D)** Bar plots showing regulatory potential of prioritized ligands for APRIL expression in FMs calculated in NicheNet analysis. **(E)** Volcano plot showing DEGs of PB cells between FM and non-FM-FLAMEs. Genes with an adjusted *P* value of <0.05 and log2-transformed fold change of ≤0.1 or ≥0.1were highlighted by red or blue dots, respectively. **(F)** NicheNet analysis of CosMx SMI data using only cells in CN1 identifying ligands predicted to regulate phenotype of PB cells in the FM-FLAME compared with non-FM-FLAMEs. Dot plots show expression of ligand-coding genes across sender cell subsets. **(G-H)** Bubble plots summarizing significantly enriched ligand–receptor interactions targeting PB cells mediated by macrophage subsets in snRNA-seq (G) and CosMx SMI data using only cells in CN1 (H).

**Figure S8: Clinicopathological relevance of FLAMEs in FL. (A–K)** Associations between FLAMEs and clinical characteristics: age (A), gender (B), hemoglobin level (C), lactate dehydrogenase level (D), number of nodal sites (E), Ann Arbor stage (F), FLIPI risk group (G), B symptoms (H), bulky disease (I), ≥3 nodal sites with each node >3 cm (J), and symptomatic splenomegaly (K). **(L)** Kaplan–Meier curves of EFS according to FLAMEs in the overall FL cohort (left), patients treated with IC (center), and patients managed with AS (right) (two-sided log-rank test). For A–K, overall differences were assessed using chi-square or Fisher's exact tests, as appropriate. Asterisks indicate significance based on two-sided Wilcoxon rank-sum test comparing each group versus all others with Benjamini–Hochberg correction (*FDR < 0.05, **FDR < 0.01, ***FDR < 0.001). White and black asterisks indicate significantly over- and underrepresented niches, respectively.

**Figure S9: Clinicopathological relevance of intrafollicular macrophage percentage (IFMP) in an independent FL SPI cohort. (A)** Receiver operating characteristic curves of IFMP for predicting the FM-FLAME in CosMx SMI data using macrophage subsets included in the intrafollicular archetype analysis. AUC, area under the curve. **(B–H)** Associations between IFMP and clinical characteristics in the SPI cohort: age (B), hemoglobin level (C), lactate dehydrogenase level (D), Ann Arbor stage (E), FLIPI risk group (F), treatment approaches (G), and IC regimen (H). **(I)** Proportion of PB cells among B cells (left) and all cells (right) across IFMP groups. **(J)** Proportion of PB plus quiescent B (QB) cells among all cells between high and low IFMP groups. **(K)** Representative multiplex SPI data showing different BCL2 protein status between high and low IFMP FL samples. Two-sided Wilcoxon rank-sum test was used in I and J. For B–H, n, and o, overall differences were assessed using chi-square or Fisher's exact tests, as appropriate. Asterisks indicate significant over- or

underrepresentation based on standardized residuals with Benjamini–Hochberg correction (*FDR < 0.05, ***FDR < 0.001). White and black asterisks indicate over- and underrepresented categories, respectively.

## REFERENCES


1 Chihara, D. *et al*. Real-world treatment patterns and clinical outcomes in patients with follicular lymphoma: a SEER-Medicare analysis. *Blood Neoplasia* **2**, 100080 (2025). https://doi.org/10.1016/j.bneo.2025.100080

2 Dreyling, M. *et al*. Newly diagnosed and relapsed follicular lymphoma: ESMO Clinical Practice Guidelines for diagnosis, treatment and follow-up. *Ann Oncol* **32**, 298-308 (2021). https://doi.org/10.1016/j.annonc.2020.11.008

3 Shadman, M. *et al*. Treatment of Follicular Lymphoma With CHOP and Anti-CD20 Therapy: 15-Year Follow-Up of the SWOG S0016 Trial. *JAMA Oncol* **12**, 394-401 (2026). https://doi.org/10.1001/jamaoncol.2026.0042

4 Maurer, M. J. *et al*. Early event status informs subsequent outcome in newly diagnosed follicular lymphoma. *Am J Hematol* **91**, 1096-1101 (2016). https://doi.org/10.1002/ajh.24492

5 Day, J. R. *et al*. Treatment patterns and outcomes in follicular lymphoma with POD24: an analysis from the LEO Consortium. *Blood Adv* **9**, 1013-1023 (2025). https://doi.org/10.1182/bloodadvances.2024014053

6 Casulo, C. *et al*. Validation of POD24 as a robust early clinical end point of poor survival in FL from 5225 patients on 13 clinical trials. *Blood* **139**, 1684-1693 (2022). https://doi.org/10.1182/blood.2020010263

7 Pastore, A. *et al*. Integration of gene mutations in risk prognostication for patients receiving first-line immunochemotherapy for follicular lymphoma: a retrospective analysis of a prospective clinical trial and validation in a population-based registry. *Lancet Oncol* **16**, 1111-1122 (2015). https://doi.org/10.1016/S1470-2045(15)00169-2

8 Huet, S. *et al*. A gene-expression profiling score for prediction of outcome in patients with follicular lymphoma: a retrospective training and validation analysis in three international cohorts. *Lancet Oncol* **19**, 549-561 (2018). https://doi.org/10.1016/S1470-2045(18)30102-5

9 Campo, E. *et al*. The International Consensus Classification of Mature Lymphoid Neoplasms: a report from the Clinical Advisory Committee. *Blood* **140**, 1229-1253 (2022). https://doi.org/10.1182/blood.2022015851

10 Alaggio, R. *et al*. The 5th edition of the World Health Organization Classification of Haematolymphoid Tumours: Lymphoid Neoplasms. *Leukemia* **36**, 1720-1748 (2022). https://doi.org/10.1038/s41375-022-01620-2

11 Han, G. *et al*. Follicular lymphoma microenvironment characteristics associated with tumor cell mutations and MHC class II expression. *Blood Cancer Discov* **3**, 428-443 (2022). https://doi.org/10.1158/2643-3230.BCD-21-0075

12 Abe, Y. *et al*. Distinct follicular T cell subsets regulate lymphoma progression and outcomes. *Cancer cell* **43**, 1850-1865 e1811 (2025). https://doi.org/10.1016/j.ccell.2025.06.013

13 Andor, N. *et al*. Single-cell RNA-Seq of follicular lymphoma reveals malignant B-cell types and coexpression of T-cell immune checkpoints. *Blood* **133**, 1119-1129 (2019). https://doi.org/10.1182/blood-2018-08-862292

14 Roider, T. *et al*. Dissecting intratumour heterogeneity of nodal B-cell lymphomas at the transcriptional, genetic and drug-response levels. *Nat Cell Biol* **22**, 896-906 (2020). https://doi.org/10.1038/s41556-020-0532-x

15 Dai, Y. *et al*. Multi-modal spatial characterization of tumor immune microenvironments identifies targetable inflammatory niches in diffuse large B cell lymphoma. *Nature genetics* **57**, 2715-2727 (2025). https://doi.org/10.1038/s41588-025-02353-5

16 Cerhan, J. R. *et al*. The Lymphoma Epidemiology of Outcomes cohort study: Design, baseline characteristics, and early outcomes. *Am J Hematol* **99**, 408-421 (2024). https://doi.org/10.1002/ajh.27202

17 Gunn, M. D. *et al*. A B-cell-homing chemokine made in lymphoid follicles activates Burkitt's lymphoma receptor-1. *Nature* **391**, 799-803 (1998). https://doi.org/10.1038/35876

18 Legler, D. F. *et al*. B cell-attracting chemokine 1, a human CXC chemokine expressed in lymphoid tissues, selectively attracts B lymphocytes via BLR1/CXCR5. *J Exp Med* **187**, 655-660 (1998). https://doi.org/10.1084/jem.187.4.655

19 Mueller, S. N. & Germain, R. N. Stromal cell contributions to the homeostasis and functionality of the immune system. *Nat Rev Immunol* **9**, 618-629 (2009). https://doi.org/10.1038/nri2588

20 Roozendaal, R. & Mebius, R. E. Stromal cell-immune cell interactions. *Annu Rev Immunol* **29**, 23-43 (2011). https://doi.org/10.1146/annurev-immunol-031210-101357

21 Sangaletti, S. *et al*. Macrophage-derived SPARC bridges tumor cell-extracellular matrix interactions toward metastasis. *Cancer Res* **68**, 9050-9059 (2008). https://doi.org/10.1158/0008-5472.Can-08-1327

22 Noy, R. & Pollard, J. W. Tumor-associated macrophages: from mechanisms to therapy. *Immunity* **41**, 49-61 (2014). https://doi.org/10.1016/j.immuni.2014.06.010

23 Zhao, T., Su, Z., Li, Y., Zhang, X. & You, Q. Chitinase-3 like-protein-1 function and its role in diseases. *Signal Transduct Target Ther* **5**, 201 (2020). https://doi.org/10.1038/s41392-020-00303-7

24 Li, T. J. *et al*. SIGLEC15 amplifies immunosuppressive properties of tumor-associated macrophages in pancreatic cancer. *Cancer Lett* **530**, 142-155 (2022). https://doi.org/10.1016/j.canlet.2022.01.026

25 Mulder, K. *et al*. Cross-tissue single-cell landscape of human monocytes and macrophages in health and disease. *Immunity* **54**, 1883-1900 e1885 (2021). https://doi.org/10.1016/j.immuni.2021.07.007

26 Abe, Y. *et al*. Distinct follicular T cell subsets regulate lymphoma progression and outcomes. *Cancer Cell* (2025). https://doi.org/10.1016/j.ccell.2025.06.013

27 Browaeys, R., Saelens, W. & Saeys, Y. NicheNet: modeling intercellular communication by linking ligands to target genes. *Nature methods* **17**, 159-162 (2020). https://doi.org/10.1038/s41592-019-0667-5

28 Elgueta, R. *et al*. Molecular mechanism and function of CD40/CD40L engagement in the immune system. *Immunol Rev* **229**, 152-172 (2009). https://doi.org/10.1111/j.1600-065X.2009.00782.x

29 Cannarile, M. A. *et al*. Colony-stimulating factor 1 receptor (CSF1R) inhibitors in cancer therapy. *J Immunother Cancer* **5**, 53 (2017). https://doi.org/10.1186/s40425-017-0257-y

30 Mackay, F. & Schneider, P. Cracking the BAFF code. *Nat Rev Immunol* **9**, 491-502 (2009). https://doi.org/10.1038/nri2572

31 He, B. *et al*. Lymphoma B cells evade apoptosis through the TNF family members BAFF/BLyS and APRIL. *J Immunol* **172**, 3268-3279 (2004). https://doi.org/10.4049/jimmunol.172.5.3268

32 Gupta, M. *et al*. A proliferation-inducing ligand mediates follicular lymphoma B-cell proliferation and cyclin D1 expression through phosphatidylinositol 3-kinase-regulated mammalian target of rapamycin activation. *Blood* **113**, 5206-5216 (2009). https://doi.org/10.1182/blood-2008-09-179762

33 Carbone, A. *et al*. Follicular lymphoma. *Nat Rev Dis Primers* **5**, 83 (2019). https://doi.org/10.1038/s41572-019-0132-x

34 Horn, H. *et al*. Follicular lymphoma grade 3B is a distinct neoplasm according to cytogenetic and immunohistochemical profiles. *Haematologica* **96**, 1327-1334 (2011). https://doi.org/10.3324/haematol.2011.042531

35 Wahlin, B. E. *et al*. Clinical significance of the WHO grades of follicular lymphoma in a population-based cohort of 505 patients with long follow-up times. *British journal of haematology* **156**, 225-233 (2012). https://doi.org/10.1111/j.1365-2141.2011.08942.x

36 Barraclough, A. *et al*. Outcomes in grade 3B follicular lymphoma: an international study led by the Australasian Lymphoma Alliance. *Haematologica* **108**, 2444-2453 (2023). https://doi.org/10.3324/haematol.2022.281375

37 Brice, P. *et al*. Comparison in low-tumor-burden follicular lymphomas between an initial no-treatment policy, prednimustine, or interferon alfa: a randomized study from the Groupe d'Etude des Lymphomes Folliculaires. Groupe d'Etude des Lymphomes de l'Adulte. *J Clin Oncol* **15**, 1110-1117 (1997). https://doi.org/10.1200/jco.1997.15.3.1110

38 Krishnamurty, A. T. & Turley, S. J. Lymph node stromal cells: cartographers of the immune system. *Nature immunology* **21**, 369-380 (2020). https://doi.org/10.1038/s41590-020-0635-3

39 Heesters, B. A., Myers, R. C. & Carroll, M. C. Follicular dendritic cells: dynamic antigen libraries. *Nature reviews. Immunology* **14**, 495-504 (2014). https://doi.org/10.1038/nri3689

40 Crotty, S. T Follicular Helper Cell Biology: A Decade of Discovery and Diseases. *Immunity* **50**, 1132-1148 (2019). https://doi.org/10.1016/j.immuni.2019.04.011

41 Carlsen, H. S., Baekkevold, E. S., Morton, H. C., Haraldsen, G. & Brandtzaeg, P. Monocyte-like and mature macrophages produce CXCL13 (B cell-attracting chemokine 1) in inflammatory lesions with lymphoid neogenesis. *Blood* **104**, 3021-3027 (2004). https://doi.org/10.1182/blood-2004-02-0701

42 Xie, Y. *et al*. M2 macrophages secrete CXCL13 to promote renal cell carcinoma migration, invasion, and EMT. *Cancer Cell Int* **21**, 677 (2021). https://doi.org/10.1186/s12935-021-02381-1

43 Yang, M. *et al*. CXCL13 shapes immunoactive tumor microenvironment and enhances the efficacy of PD-1 checkpoint blockade in high-grade serous ovarian cancer. *J Immunother Cancer* **9** (2021). https://doi.org/10.1136/jitc-2020-001136

44 Aoki, T. *et al*. Spatially Resolved Tumor Microenvironment Predicts Treatment Outcomes in Relapsed/Refractory Hodgkin Lymphoma. *J Clin Oncol* **42**, 1077-1087 (2024). https://doi.org/10.1200/jco.23.01115

45 WHO Classification of Tumours Editorial Board. *Haematolymphoid Tumours*. 5th edn, (International Agency for Research on Cancer, 2024).

46 Canioni, D. *et al*. High numbers of tumor-associated macrophages have an adverse prognostic value that can be circumvented by rituximab in patients with follicular lymphoma enrolled onto the GELA-GOELAMS FL-2000 trial. *J Clin Oncol* **26**, 440-446 (2008). https://doi.org/10.1200/jco.2007.12.8298

47 Merryman, R. *et al*. Consensus recommendations from the 2024 International Follicular Lymphoma Scientific Workshop. *Blood Adv* **10**, 1591-1602 (2026). https://doi.org/10.1182/bloodadvances.2025018079

48 Campo, E. *et al*. The 2008 WHO classification of lymphoid neoplasms and beyond: evolving concepts and practical applications. *Blood* **117**, 5019-5032 (2011). https://doi.org/10.1182/blood-2011-01-293050

49 Li, X. *et al*. Large B cell lymphoma microenvironment archetype profiles. *Cancer cell* **43**, 1347-1364 e1313 (2025). https://doi.org/10.1016/j.ccell.2025.06.002

50 He, S. *et al*. High-plex imaging of RNA and proteins at subcellular resolution in fixed tissue by spatial molecular imaging. *Nature biotechnology* **40**, 1794-1806 (2022). https://doi.org/10.1038/s41587-022-01483-z

51 Abe, Y. *et al*. A single-cell atlas of non-haematopoietic cells in human lymph nodes and lymphoma reveals a landscape of stromal remodelling. *Nat Cell Biol* **24**, 565-578 (2022). https://doi.org/10.1038/s41556-022-00866-3

# Figures

## Figure 1

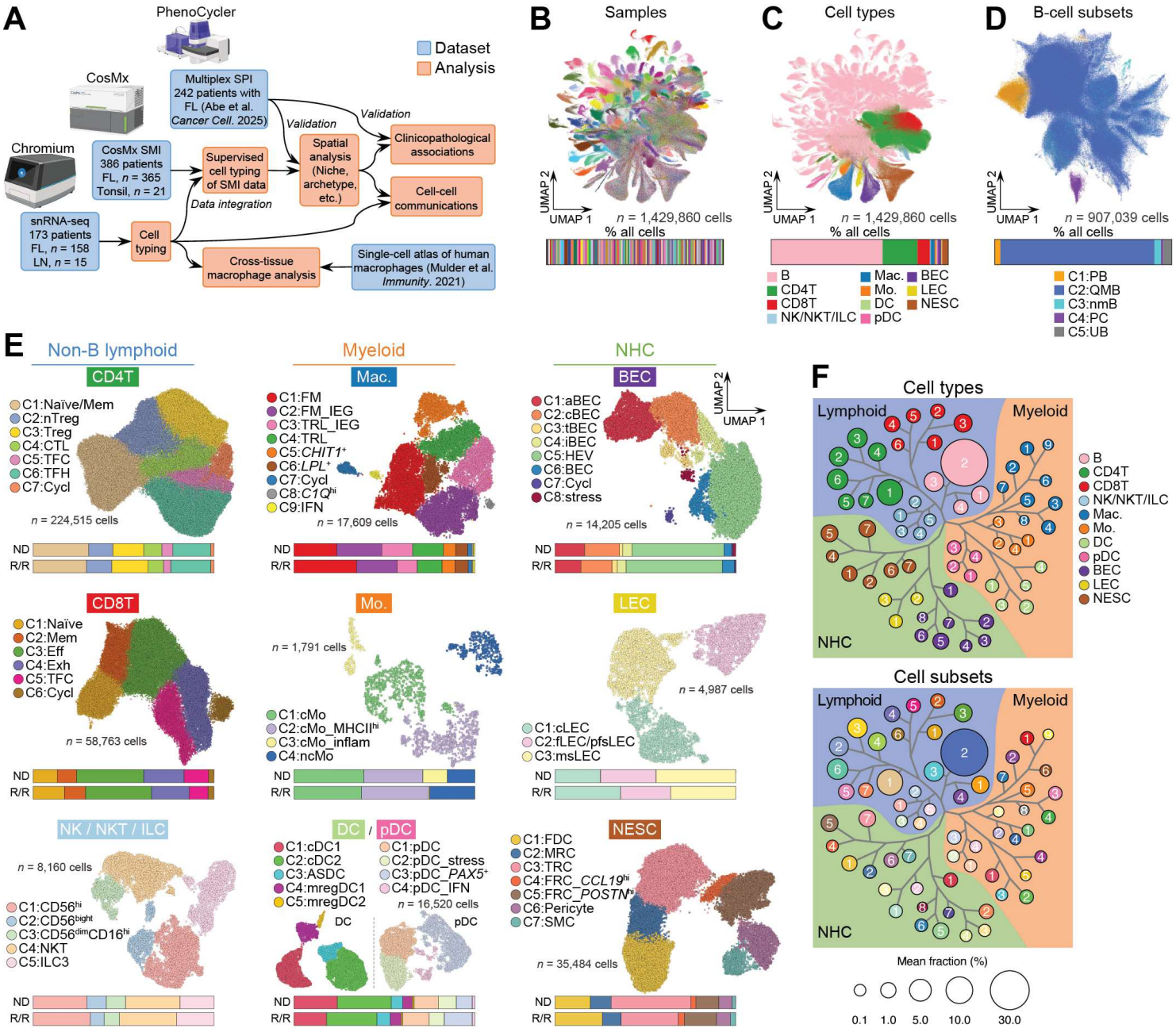


Figure 1

**snRNA-seq atlas of follicular lymphoma (FL). (A)** Schematic overview of the study design and patient cohorts for snRNA-seq, CosMx spatial molecular imaging (SMI), and multiplex spatial protein imaging (SPI). LN, lymph node. **(B-C)** UMAP projection of all cells analyzed by snRNA-seq and bar plots showing the proportions of cells colored by sample identity (B) and cell types (C). **(D)** UMAP projection of B cells colored by subsets. **(E)** UMAP projection of non-B cell populations, showing subsets identified by

unsupervised clustering. Stacked bar plots indicate proportions of each subset in newly diagnosed (ND) or relapsed/refractory (R/R) FL samples. **(F)** Dendrogram of cell subsets following hierarchical clustering of transcriptomic similarity. The background is colored by cell lineages, and the nodes are colored by cell type (top) or subset (bottom). Node size is proportional to the fraction of each cell subset relative to all cells.

## Figure 2

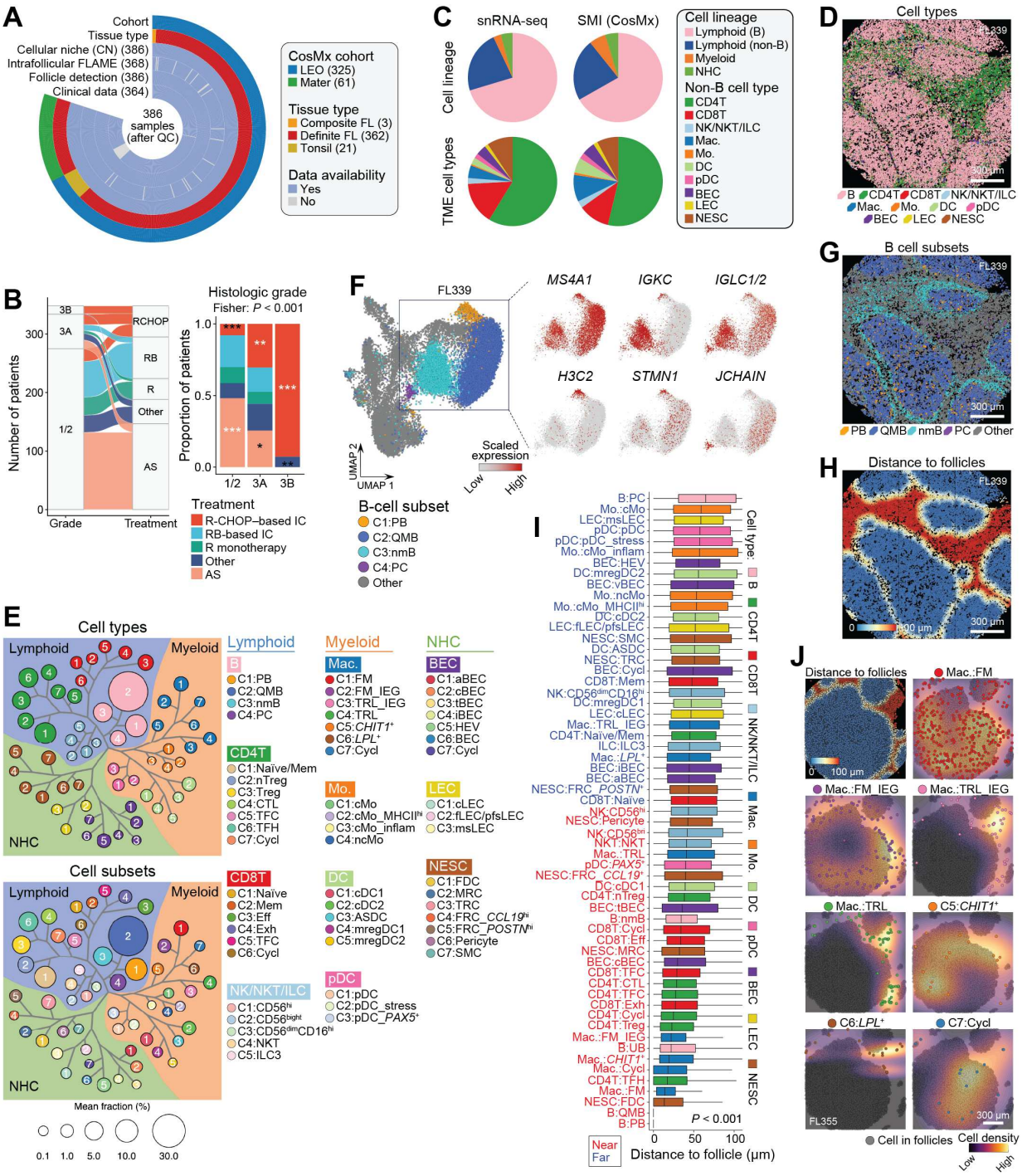


## Figure 2

**Spatial single-cell atlas of FL. (A)** Circular plot summarizing the composition of the CosMx SMI cohort and associated sample-level annotations. **(B)** Alluvial (left) and stacked bar (right) plots showing the association between histologic grades and treatment approach in patients with FL from the CosMx SMI cohort. Overall differences were assessed using Fisher's exact test. Asterisks indicate significant over- (black) or under- (white) representation based on standardized residuals with Benjamini–Hochberg correction (**FDR < 0.01, ***FDR < 0.001). R-CHOP, rituximab, cyclophosphamide, doxorubicin, vincristine, and prednisone; RB, rituximab-bendamustine; IC, immunochemotherapy; AS, active surveillance. **(C)** Pie charts showing the composition of cell lineages (top) and non-B cell types (bottom) in snRNA-seq (left) and CosMx SMI (right) data. **(D)** Representative spatial distribution of cells colored by cell types. **(E)** Dendrogram of cell subsets following hierarchical clustering of transcriptomic similarity in CosMx SMI data. The background is colored by cell lineages, and the nodes are colored by cell types (top) or cell subsets (bottom). Node size is proportional to the fraction of each cell subset relative to all cells. **(F)** UMAP projection and expression of key markers in cells from a representative FL sample from CosMx SMI data, highlighting B cell subsets identified by sample-level unsupervised clustering. **(G)** Representative spatial distribution of B cell subsets in FL. **(H)** Representative spatial distribution of cells, colored by minimal distance to follicles. **(I)** Sample-level median minimal distances to follicles across cell subsets in FL samples (Kruskal–Wallis test). **(J)** Representative spatial distribution patterns of macrophage subsets relative to follicles.

## Figure 3

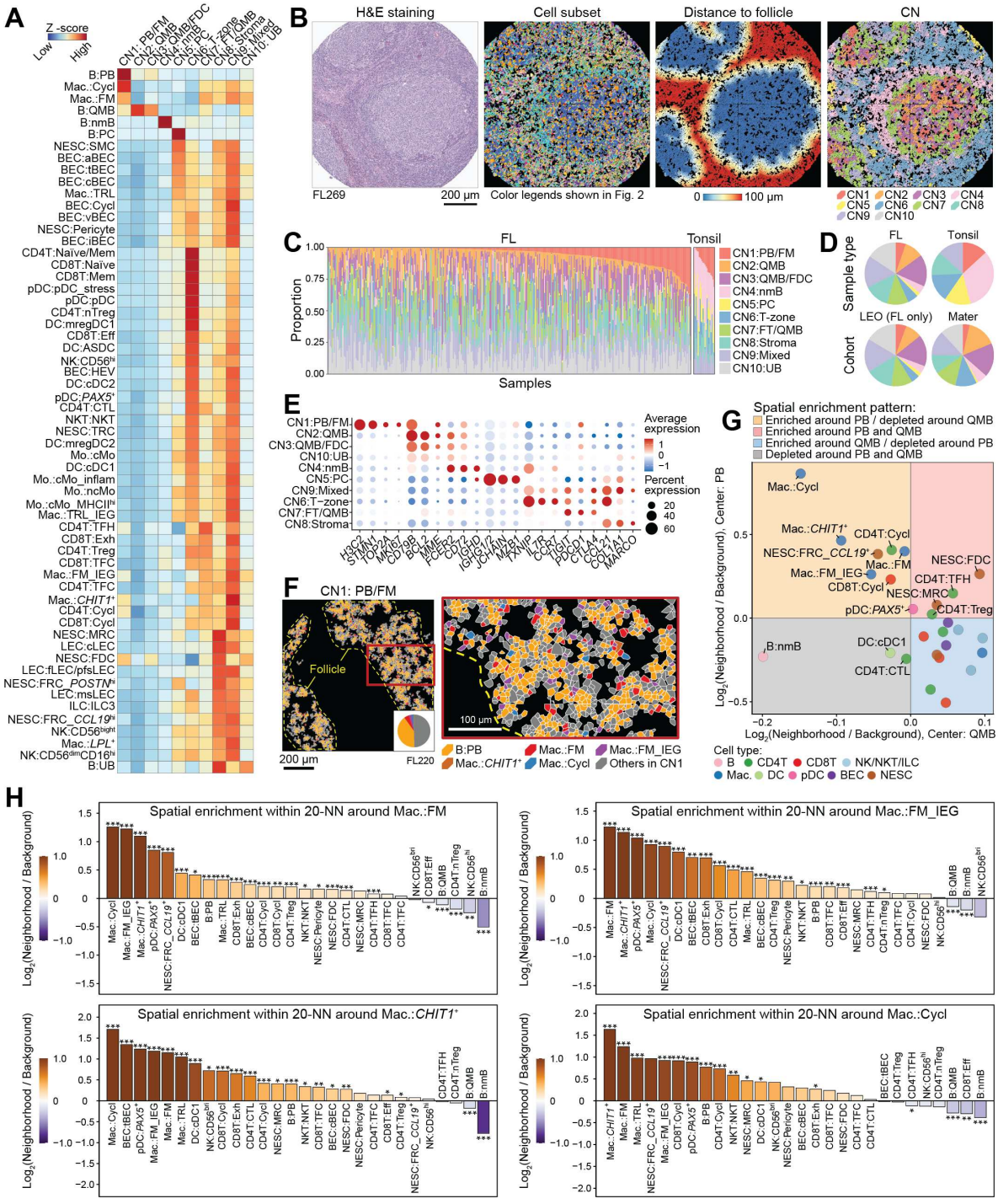


## Figure 3

**Quantitative profiles of spatial cellular niches in FL. (A)** Heatmap showing the composition of cell subsets across cellular niches (CNs) identified in CosMx SMI data. **(B)**Representative hematoxylin and eosin (H&E)-stained tissue section and corresponding CosMx SMI data showing the spatial distribution of cells colored by cell subset, distances to follicles, and CNs (left to right). **(C)**Proportion of each CN across FL and tonsil samples. **(D)** Pie charts showing the average CN composition by sample type (top)

and cohort (bottom). **(E)**Expression of key genes across CNs. **(F)** Representative spatial distribution of CN1 (left) and a magnified view (right) highlighting key cell subsets. Pie chart shows the composition of major cell subsets within CN1. Yellow dashed lines mark follicle boundaries. **(G)** Scatter plot showing log2 ratios of 20-nearest neighbor cell subset proportions around PB and QMB cells relative to background composition in intrafollicular regions. Analyses were restricted to the top 50% of cell subsets ranked by increasing distance to the follicle (**Figure 2I**, red). **(H)** Bar plots showing log2 ratios of 20-nearest neighbor cell subset proportions around macrophage subsets relative to background composition in intrafollicular regions.

## Figure 4

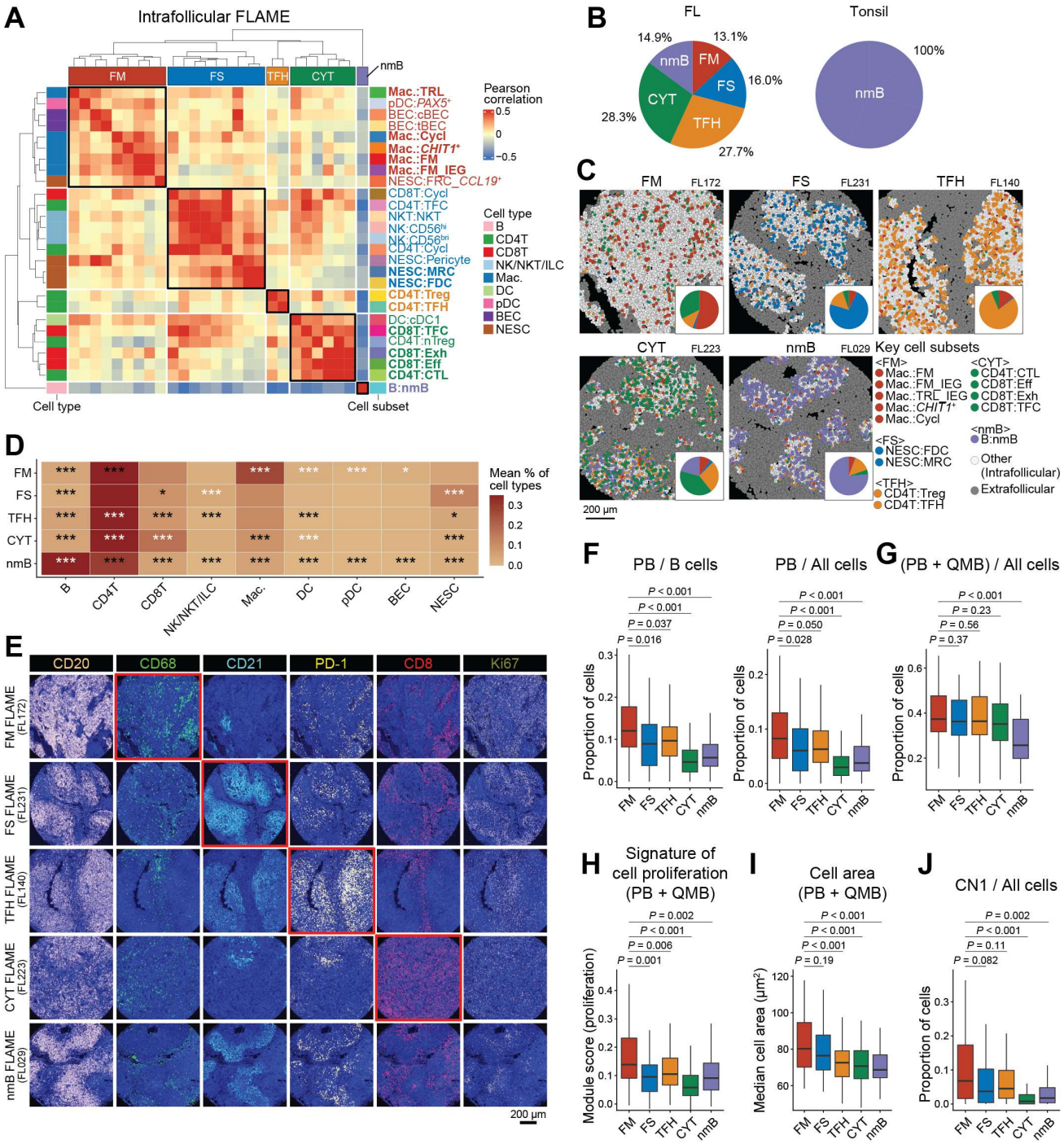


## Figure 4

**Non-negative matrix factorization of intrafollicular FL Archetype of MicroEnvironment (FLAME). (A)** Pearson correlation matrix of intrafollicular LME cell subset compositions, with modules (FLAMEs) identified by non-negative matrix factorization. **(B)** Pie charts showing the prevalence of FLAMEs in FL (left) and control tonsil (right) samples in CosMx SMI cohort. **(C)** Representative spatial distributions showing intrafollicular enrichment of key cell subsets in each FLAME. Pie charts indicate the

composition of key cell subsets in intrafollicular regions. **(D)**Heatmap showing mean cell type proportions within each FLAME. White and black asterisks indicate significant over- and underrepresentation, respectively, compared with all other FLAMEs (Welch's t test with Benjamini–Hochberg correction: *FDR < 0.05, **FDR < 0.01, ***FDR < 0.001). **(E)**Representative multiplex SPI data for each FLAME case shown in **C**, highlighting enrichment of key cell types (red squares). **(F)** Proportion of PB cells among B cells (left) and all cell (right) across FLAMEs. **(G)**Proportion of PB plus QMB cells among all cells across FLAMEs. **(H)**Sample-level median proliferation signature scores of PB and QMB cells across FLAMEs. The proliferation signature consists of top 100 DEGs in PB cells. **(I)**Sample-level median cell areas of PB and QMB cells across FLAMEs. **(J)**Proportion of cells in CN1 (PB/FM niche) among all cells across FLAMEs. Pairwise two-sided Wilcoxon rank-sum test was used in F–J.

## Figure 5

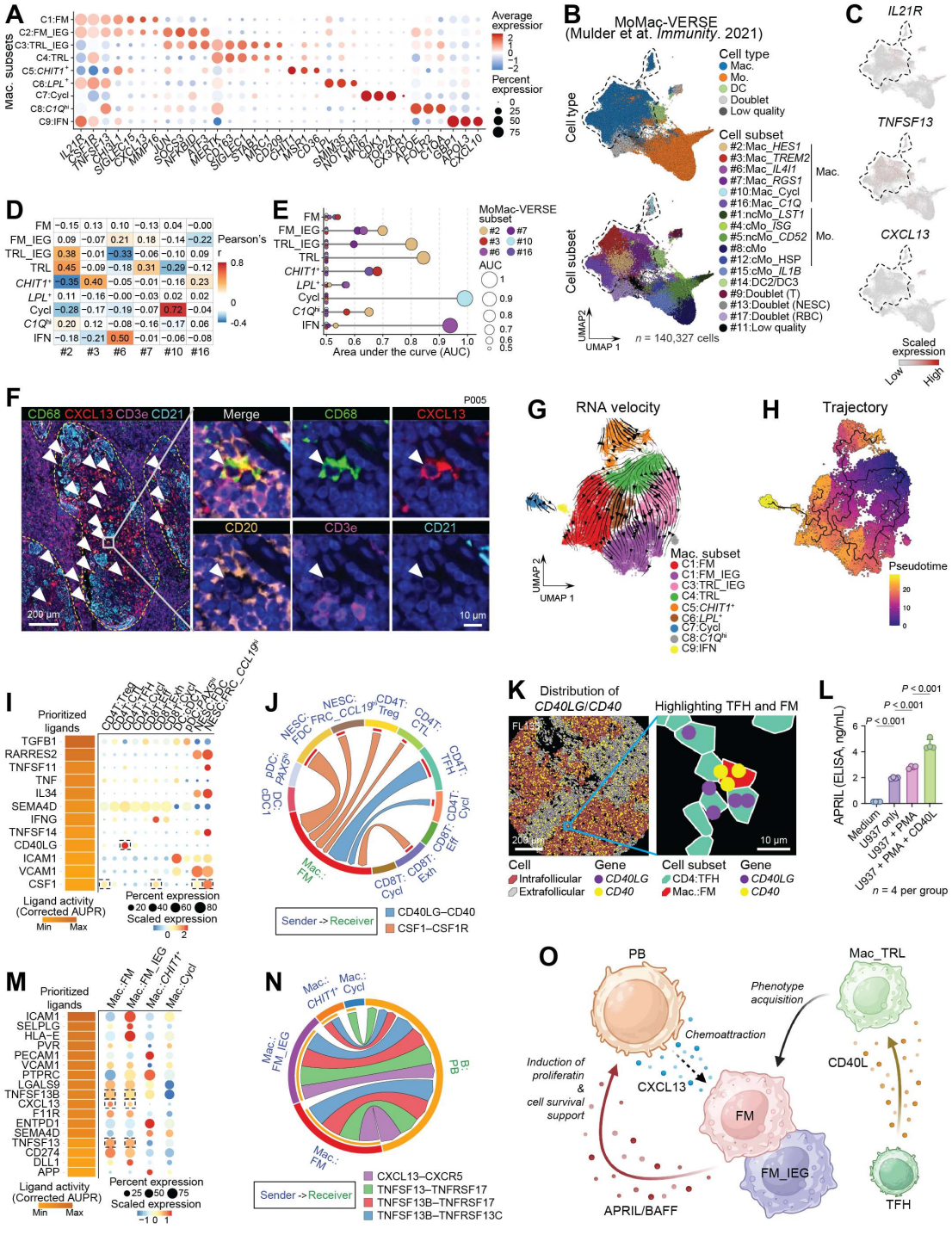


## Figure 5

**Transcriptional distinctness, differentiation, and cell-cell communications of follicular macrophages.** **(A)**Bubble plots showing expression of key genes across macrophage subsets in snRNA-seq data. **(B)** UMAP projection of the MoMac-VERSE colored by described cell types (top) and subsets (bottom). Dashed lines outline the macrophage compartment. **(C)** Expression of key functional markers of follicular macrophages (FMs) in the MoMac-VERSE. **(D)** Pearson correlation of pseudobulk expression

profiles between FL and MoMac-VERSE macrophage subsets. **(E)** Area under the receiver operating characteristic curve (AUC) of each FL macrophage signature for identifying each MoMac-VERSE macrophage subset versus all remaining subsets (one-versus-rest classification). Dot size is proportional to the AUC. AUC values below 0.5 were truncated to 0.5. **(F)**CXCL13-expressing macrophages (white arrowheads) detected by multiplex SPI in FL (Abe et al. *Cancer Cell*. 2025). Blue, DAPI. CD20 signal is omitted from the merged panel for clarity (left). **(G)** RNA velocity analysis of macrophage subsets in snRNA-seq data. **(H)** Trajectory inference and pseudotime analysis of macrophage subsets using Monocle 3. **(I)** NicheNet analysis of snRNA-seq data identifying ligands predicted to regulate FMs, prioritized by area under the precision–recall (AUPR) curve, with corresponding expression of ligand-coding genes across sender cell subsets. LME cell subsets enriched around FMs (**Figure 3H**) were analyzed. Dashed lines highlight key interactions that are consistent between snRNA-seq and SMI datasets. **(J)**Circos plot highlighting CD40LG–CD40 and CSF1–CSF1R interactions between sender cell subsets and FMs based on CellPhoneDB analysis of snRNA-seq data. Ribbon widths indicate interaction strength (scaled mean), and sector widths represent the summed interaction strengths for each cell subset. **(K)**Representative spatial distribution of *CD40LG* and *CD40*. Magnified image (right) highlighting proximal TFH cells and FMs expressing *CD40LG*and *CD40*, respectively. **(L)** APRIL (TNFSF13) levels measured by ELISA in conditioned media from U937 cells cultured with or without PMA (200 ng/mL) and/or CD40L stimulation (100 ng/mL) for 120 hours (one-way ANOVA followed by Šídák's multiple comparisons test). Data are presented as mean ± SD. **(M)** NicheNet analysis of snRNA-seq data identifying ligands from key macrophage subsets predicted to regulate phenotype of PB cells in the FM-FLAME compared with non-FM-FLAMEs. Dot plots show expression of ligand-coding genes across sender cell subsets. **(N)** Circos plot highlighting key interactions between sender macrophage subsets and PB cells based on CellPhoneDB analysis of snRNA-seq data. **(O)** Proposed model of cellular ecosystems in FL. CD40L from TFH cells promotes tissue-resident–like macrophages to acquire FM phenotypes, which in turn support proliferative phenotypes of PB cells.

## Figure 6

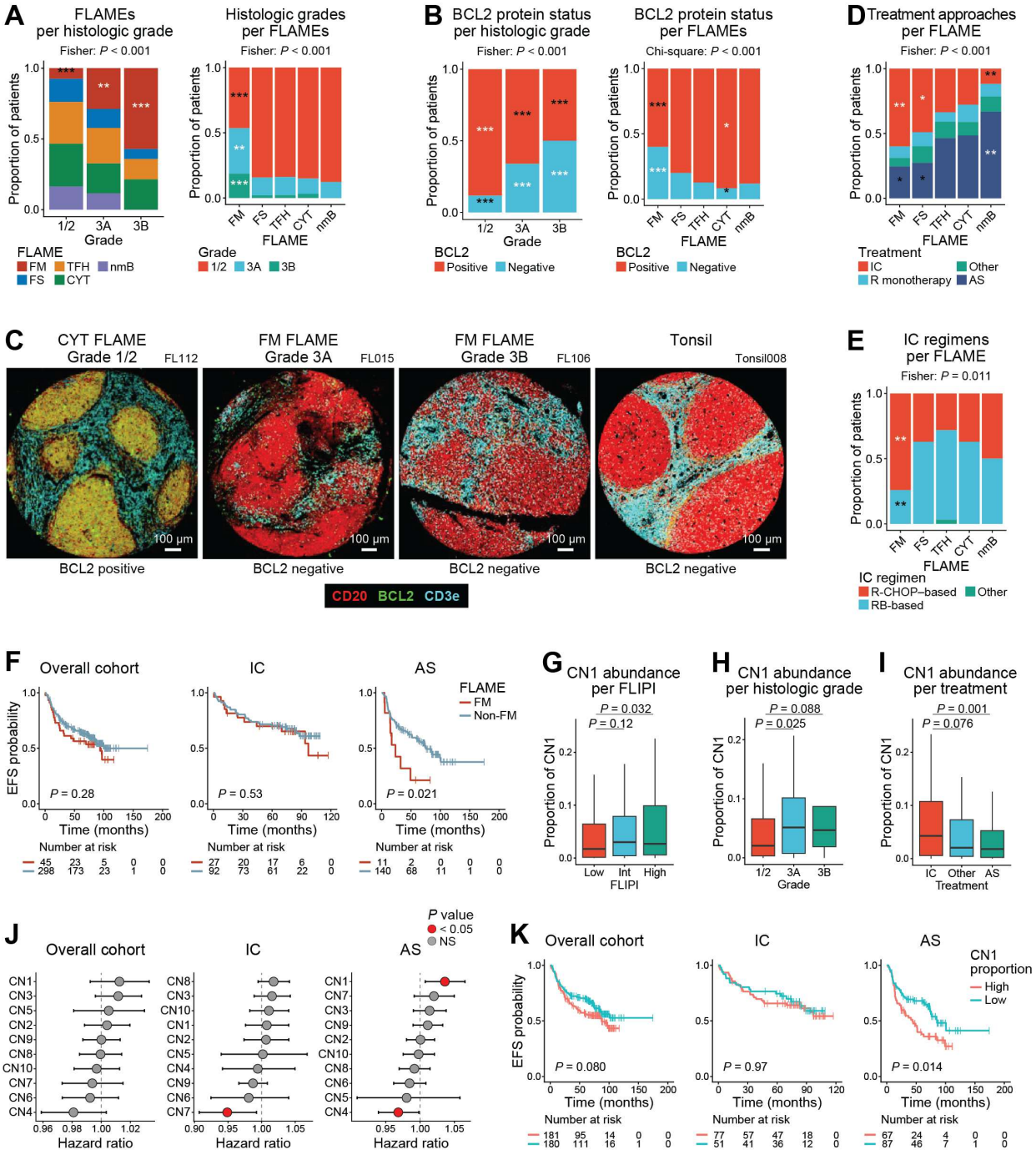


## Figure 6

**Clinicopathological associations of macrophage-enriched microenvironment in FL. (A)** Distribution of FLAMEs across histologic grades (left) and distribution of histologic grades across FLAMEs (right). **(B)** Distribution of BCL2 protein expression status across histologic grades (left) and FLAMEs (right). **(C)** Representative multiplex SPI data showing different BCL2 protein status across FL and tonsil samples in the CosMx SMI cohort. **(D)** Distribution of treatment approaches across FLAMEs. IC,

immunochemotherapy; AS, active surveillance. **(E)**Distribution of IC regimens across FLAMEs. **(F)** Kaplan–Meier curves of event-free survival (EFS) according to FM or non-FM-FLAME in the overall FL cohort (left), patients treated with IC (center), and patients managed with AS (right). **(G–I)** Proportion of cells in CN1 (PB/FM niche) among all cells stratified by FLIPI risk group (G), histologic grade (H), and treatment approach (I) (two-sided Wilcoxon rank-sum test). **(J)** Forest plots of univariable Cox proportional hazards models for EFS based on sample-level CN proportions in the overall FL cohort (left), patients treated with IC (center), and patients managed with AS (right). CN proportions were analyzed as continuous variables. Circle colors indicate statistical significance (two-sided Wald test). NS, not significant. **(K)** EFS according to CN1 abundance in the overall FL cohort (left), patients treated with IC (center), and patients managed with AS (right). Patients were dichotomized at the median CN1 abundance in the overall cohort. For F and K, two-sided log-rank test was used. For A, B, D, and E, overall differences were assessed using chi-square or Fisher's exact tests. Asterisks indicate significant over- or underrepresentation based on standardized residuals with Benjamini–Hochberg correction (*FDR < 0.05, **FDR < 0.01, ***FDR < 0.001). White and black asterisks indicate over- and underrepresentation, respectively.

## Figure 7

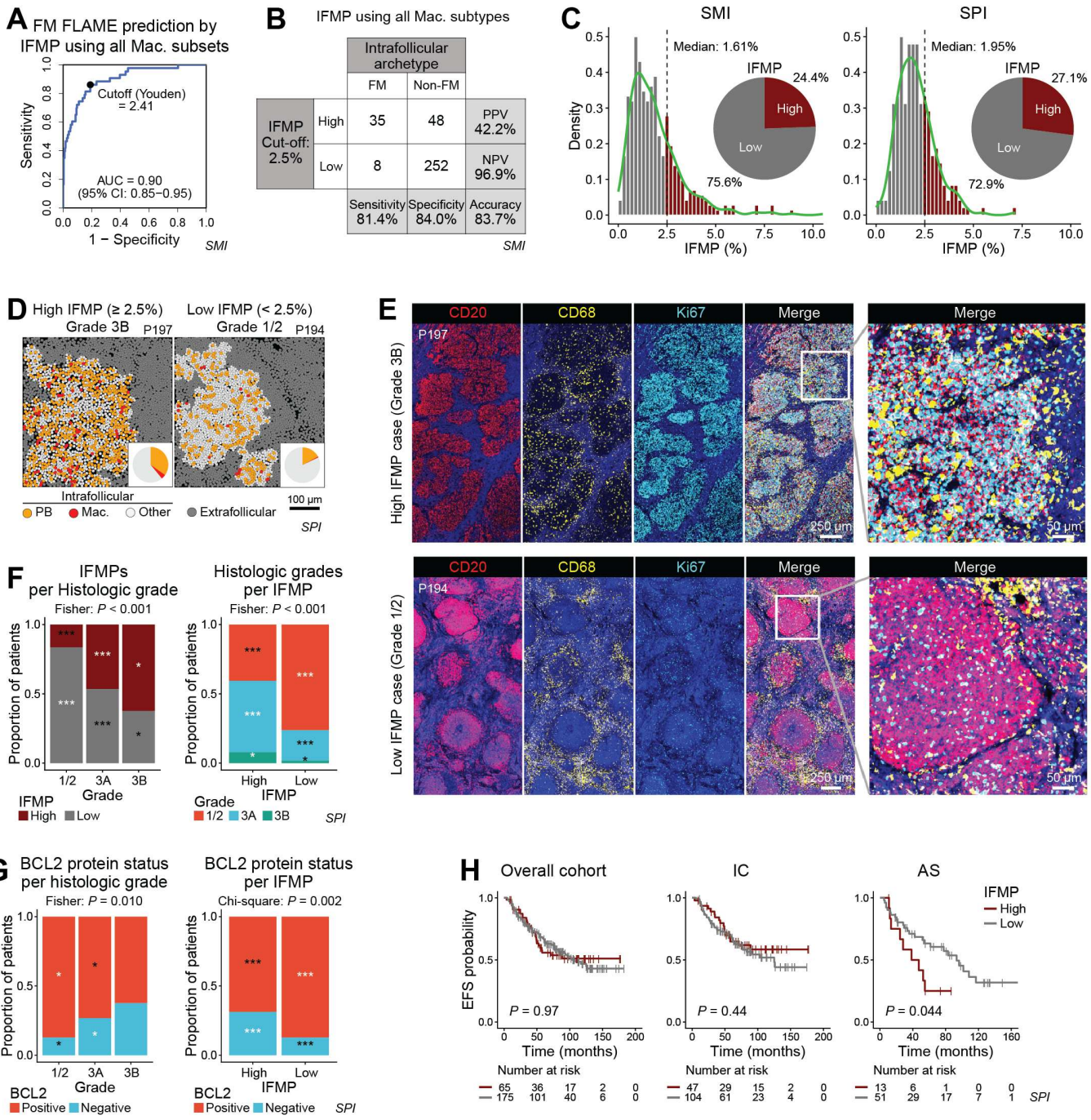


## Figure 7

**Orthogonal validation of FM-FLAME using intrafollicular macrophage percentage (IFMP) in an independent FL SPI cohort. (A)** Receiver operating characteristic curves of intrafollicular macrophage percentage (IFMP) for predicting the FM-FLAME in CosMx SMI data using all macrophage subsets. AUC, area under the curve. **(B)**Confusion matrix summarizing predictive performance in CosMx SMI data, including sensitivity, specificity, accuracy, and positive (PPV) and negative (NPV) predictive values for FM

versus non-FM-FLAMEs based on high (≥2.5%) or low (<2.5%) IFMP. **(C)** Histograms showing the distribution of IFMP in CosMx SMI and multiplex spatial protein imaging (SPI) data. Pie charts show the proportion of high and low IFMP cases. **(D)** Representative spatial distributions of cells in high (left) and low (right) IFMP cases in the SPI FL dataset (Abe et al. *Cancer Cell*. 2025), highlighting intrafollicular PB cells and macrophages. Pie charts indicate intrafollicular cellular composition. **(E)** Representative SPI of high (top) and low (bottom) IFMP cases with histologic grades 3B and 1/2, respectively. **(F)** Distribution of high and low IFMP across histologic grades (left) and the distribution of histologic grades across IFMP groups (right) in the SPI FL dataset. **(G)**Distribution of BCL2 protein expression status across histologic grades (left) and IFMP groups (right). For F and G, overall differences were assessed using chi-square or Fisher's exact tests. Asterisks indicate significant over- or underrepresentation based on standardized residuals with Benjamini–Hochberg correction (*FDR < 0.05, **FDR < 0.01, ***FDR < 0.001). White and black asterisks indicate over- and underrepresentation, respectively. **(H)**EFS according to IFMP in the SPI FL cohort (left), patients treated with IC (center), and patients managed with AS (right) (two-sided log-rank test was used).

## Supplementary Files

This is a list of supplementary files associated with this preprint. Click to download.

- SuppleFig3.png
- SuppleFig2.png
- SuppleFig7.png
- SuppleFig5.png
- SupplementaryTablesnature20261016.xlsx
- SuppleFig6.png
- SuppleFig4.png
- SuppleFig8.png
- SuppleFig1.png
- SuppleFig9.png
- FigureS.docx